UNCLASSIFIED

SECURITY CLASSIFICATION OF THIS PAGE

AD-A233 584

2

## REPORT DOCUMENTATION PAGE

READ INSTRUCTIONS BEFORE COMPLETING FORM

1. REPORT NUMBER: ARO 23758.2-EG-F
2. GOVT ACCESSION NO.: NA
3. RECIPIENT'S CATALOG NUMBER: NA
4. TITLE (and Subtitle): Hypersonic Aerodynamics Fellowships
5. TYPE OF REPORT & PERIOD COVERED: Final Report - 15 Mar 86 - 15 Sep 89
6. PERFORMING ORG. REPORT NUMBER
7. AUTHOR(s): John D. Anderson, Jr.
8. CONTRACT OR GRANT NUMBER(s): DAAL03-86-G-0040
9. PERFORMING ORGANIZATION NAME AND ADDRESS:

Dept. of Aerospace Engineering
University of Maryland
College Park, MD 20742

10. PROGRAM ELEMENT, PROJECT, TASK AREA & WORK UNIT NUMBERS: NA
11. CONTROLLING OFFICE NAME AND ADDRESS:

U. S. Army Research Office
P. O. Box 12211
Research Triangle Park, NC 27709-2211

12. REPORT DATE: Feb. 11, 1991
13. NUMBER OF PAGES: 4
14. MONITORING AGENCY NAME & ADDRESS (if different from Controlling Office)
15. SECURITY CLASS. (of this report): UNCLASSIFIED

15a. DECLASSIFICATION/DOWNGRADING SCHEDULE

16. DISTRIBUTION STATEMENT (of this Report)

Approved for public release; distribution unlimited.

DTIC APR 01 1991 C

17. DISTRIBUTION STATEMENT (of the abstract entered in Block 20, if different from Report)

NA

18. SUPPLEMENTARY NOTES

The view, opinions and/or findings contained in this report are those of the author(s) and should not be construed as an official Department of the Army position, policy, or decision, unless so designated by other documentation.

19. KEY WORDS (Continue on reverse side if necessary and identify by block number)

Hypersonic Aerodynamics, Waveriders, Shock Waves, Vortex Flows

20. ABSTRACT (Continue on reverse side if necessary and identify by block number)

This grant was a fellowship grant, funding three graduate students in hypersonic aerodynamics. This work resulted in: (1) a new approach to hypersonic waveri r vehicles, which has lead to a family of waverider with exceptionally promising characteristics, and (2) the first data on the interaction of a vortex with a shock wave at hypersonic speeds.

DD FORM 1 JAN 73 1473 EDITION OF 1 NOV 65 IS OBSOLETE 10

UNCLASSIFIED

SECURITY CLASSIFICATION OF THIS PAGE (When Data Entered)

91 3 [illegible] 146

# HYPERSONIC AERODYNAMICS FELLOWSHIPS-- FINAL REPORT

by

John D. Anderson, Jr., Professor
Department of Aerospace Engineering
University of Maryland
College Park, Maryland 20742

This is a final report on ARO Grant DAAL03-88-G-0083. This research program was to provide graduate fellowships to students in the area of hypersonic aerodynamics. Indeed, the Army Research Office can take some pride in the fact that this funding was the leading edge of a renewed emphasis in hypersonic aerodynamics in universities during the middle 1980's, at a time when this discipline was seriously languishing. In particular, this grant served to spur the growth of the Hypersonics Group at the University of Maryland-- a group which now numbers 17 full-time graduate students. In this sense, we wish to express our gratitude to ARO for helping our graduate program in hypersonic aerodynamics in such a pivotal manner.

The following students were funded under the ARO Fellowship Program at Maryland. Also listed are their current status.

1. Dr. Kevin Bowcutt. Received his Ph.D. under the ARO Fellowship Program, and is now a lead research engineer with Rockwell in their National Aerospace Plane Program. Dr. Bowcutt was selected as the Rockwell Engineer of the Year in 1990 -- a very prestigious award for such a young engineer.

2. Dr. Griffin Corpening. Received his Ph.D. under the ARO Fellowship Program, and is now a research leader at the Johns Hopkins Applied Physics Laboratory (APL) in their hypersonic SCRAMJET program. Last year, Dr. Corpening was awarded APL's Best Paper of the Year Award, for an AIAA paper based on his Ph.D. dissertation. (This paper is included as Appendix B in this Final Report.)
3. Mr. Scott Seifert. Finished all requirements for his Ph.D. except for his Oral Comprehensive Examination and his Dissertation. Mr. Seifert is now continuing to work towards finishing these requirements, while at the same time accepting employment at the Applied Physics Laboratory.

The following accomplishments have been made as a direct result of this ARO Fellowship Grant:

1. Two Ph.D.'s and one near Ph.D have been added to the United State's engineering work force in hypersonics, at a critical time when they were badly needed. Moreover, these graduates are top-notch people -- the creme of the crop. Both Drs. Bowcutt and Corpening graduated with perfect 4.0 Grade Point Averages -- straight A's.
2. Dr. Bowcutt's Ph.D. research dealt with a new approach to hypersonic waverider design, and led to a new, unique family of hypersonic waveriders called viscous optimized waveriders. These University of Maryland waveriders have prompted a new surge in waverider activity around the country. Our waverider computer

program (MAXWARP) is now being used by 15 companies and government laboratories. Two University of Maryland waveriders have been successfully tested in the NASA Langley hypersonic wind tunnels, validating our analysis and multiplying interest in these waveriders. Langley is now embarking on their own high-priority waverider program, as a result. In October 1990, the University of Maryland hosted the 1st International Hypersonic Waverider Symposium, which was an acclaimed success. There have been three articles in Aviation Week over the past four months describing the University of Maryland Waverider Program. All of this was started with the ARO Fellowship Grant. We sincerely believe that ARO can take pride in this accomplishment -- the ARO Grant was a seed upon which a major program has been built -- a program with far-reaching results affecting many people in our national hypersonics effort.

3. Dr. Corpening's Ph.D. research was an application of computational fluid dynamics to a flow problem of interest. The flow problem was the interaction of a vortex with an oblique shock wave at hypersonic speeds. Dr.Corpening wrote his own three-dimensional, finite-volume computer program to solve this problem. The results indicated a major interaction between the vortex and the shock, the first such data at hypersonic speeds.

The details of this technical work are contained in Appendices A and B.

These are:

Appendix A: Bowcutt, K.G., Anderson, J.D. and Capriotti, D., "Viscous Optimized Hypersonic Waveriders," AIAA Paper No. 87-0272.

Appendix B: Corpening, G. and Anderson,J., "Numerical Solutions to Three-Dimensional Shock Wave/Vortex Interaction at Hypersonic Speeds," AIAA Paper No. 89-0674.

Hence, no further elaboration will be given here. The remainder of this report is represented by the technical descriptions given in Appendices A and B.

# APPENDIX A

AIAA'87

# AIAA-87-0272

# Viscous Optimized Hypersonic Waveriders

K. G. Bowcutt, J. D. Anderson and
D. Capriotti, Univ. of Maryland,
College Park, MD

**AIAA 25th Aerospace Sciences Meeting**
January 12-15, 1987/Reno, Nevada

# VISCOUS OPTIMIZED HYPERSONIC WAVERIDERS

by

Kevin G. Bowcutt,* John D. Anderson, Jr.,** and Diego Capriotti***

Department of Aerospace Engineering
University of Maryland
College Park, Maryland 20742

> *"It is really not foreseeable that an 'optimized' calculated shape could do anything more than give a guide to the designer. However, it is only a guide that the designer actually wants from the aerodynamicist. He would really be a little embarrassed to be offered a perfect aerodynamic shape, which he would then have to carve holes in, add fairings, and so on, in order to satisfy such mundane requirements as that the pilot should be able to see where he is going or that people have somewhere convenient to get in and out."*
>
> P.L. Roe
> Royal Aircraft Establishment
> January 1970

## ABSTRACT

A family of optimized hypersonic waveriders is generated and studied wherein detailed viscous effects are included within the optimization process itself. This is in contrast to previous optimized waverider work, wherein purely inviscid flow is used to obtain the waverider shapes. For the present waveriders, the undersurface is a streamsurface of an inviscid conical flowfield, the upper surface is a streamsurface of the inviscid flow over a tapered cylinder (calculated by the axisymmetric method of characteristics), and the viscous effects are treated by integral solutions of the boundary layer equations. Transition from laminar to turbulent flow is included within the viscous calculations. The optimization is carried out using a non-linear simplex method. The resulting family of viscous hypersonic waveriders yields predicted high values of lift/drag, high enough to break the "L/D barrier" based on experience with other hypersonic configurations. Moreover, the numerical optimization process for the viscous waveriders results in distinctly different shapes compared to previous work with inviscid-designed waveriders. Also, the fine details of the viscous solution, such as how the shear stress is distributed over the surface, and the location of transition, are crucial to the details of the resulting waverider geometry.

## I. INTRODUCTION

Over the past few years, interest in all aspects of hypersonic flight has grown explosively, driven by new vehicle concepts such as the National Aerospace Plane (NASP), aero-assisted orbital transfer vehicles (AOTV's), the hypersonic transport (the "Orient Express"), and hypersonic missiles, to name just a few. An extended discussion of these concepts, as well as a survey of hypersonic aerodynamic research contrasting the "old" with the "new" hypersonics, is given in Ref.1. Hence no further elaboration will be given here.

The present paper deals with a class of advanced hypersonic lifting configurations. To help understand the motivation for the present work, the following background is given. For a lifting aerodynamic body, it is well-known that high maximum lift-to-drag ratios, $(L/D)_{max}$, are very difficult to obtain at hypersonic speeds, due to the presence of strong shock waves (hence high wave drag) and massive viscous effects. At supersonic and hypersonic speeds, the most efficient lifting surface is the infinitely thin flat

---

* Graduate Hypersonic Aerodynamics Fellow, sponsored by the Army Research Office, Dr. Robert Singleton, monitor. Member, AIAA. Presently, Engineer, Rockwell International, Los Angeles.

** Professor. Fellow, AIAA. Currently on sabbatical as the Charles Lindbergh Professor at the National Air and Space Museum, Smithsonian Institution.

*** Graduate Research Assistant. Student member, AIAA.

plate; the inviscid hypersonic aerodynamic properties of a flat plate are shown as the solid curves in Fig.1, based on the Newtonian limit of free stream Mach number $M_\infty \to \infty$ and $\gamma = C_p/C_v \to 1$. Note that L/D theoretically approaches infinity as the angle-of-attack, $\alpha$, approaches zero. In reality, viscous effects will cause L/D to peak at low values of $\alpha$, and to go to zero as $\alpha \to 0$. This is illustrated by the dashed line in Fig.1, which shows the variation of L/D modified by skin friction as predicted by a reference temperature method described in Ref. 2. Although the infinitly thin flat plate shown in Fig.1 is the most effective lifting surface aerodynamically, it is the least effective in terms of volume capacity. It goes without saying that all practical flight vehicles must have a finite volume to carry fuel, payload, etc. Hence, the flat plate results, although instructive, are of academic interest only. In contrast, Fig. 2 shows values of $(L/D)_{max}$ versus the volume parameter $V^{2/3}/S$ for several generic hypersonic configurations, obtainfrom Ref. 3. Here, V is the body volume and S is the planform area. Note from Fig.2 that typical hypersonic values of $(L/D)_{max}$ range from 4 to 6 for such lifting bodies at the conditions shown. These values are also typical of the hypersonic transport configuration studied in Ref. 4. Clearly, values of $(L/D)_{max}$ for hypersonic vehicles are substantially lower than those for convenal subsonic and low supersonic airplanes. (For example, the maximum L/D values for the World War II Boeing B-29 and the contemporary General Dynamics F-111 are 16.8 and 15.8 respectively, as obtained from Ref. 5). Indeed, as $M_\infty$ increases across the supersonic and hypersonic regimes, there is a general empirical correlation for $(L/D)_{max}$ based on actual flight vehicle experience, given by Kuchemann[6]:

$$(L/D)_{max} = \frac{4(M_\infty+3)}{M_\infty}$$

This variation is shown as the solid curve in Fig.3. Also shown are a number of data points for various previous hypersonic vehicle configurations at various Reynolds numbers (the open symbols), as well as new results from the present investigation (the solid symbols). Fig. 3 is pivotal to the present paper, and will be discussed at length in subsequent sections. However, at this stage in our discussion, Fig.3 is used to illustrate only the following aspects:

1. The solid curve represents a type of "L/D barrier" for conventional hypersonic vehicles, which is difficult to break.
2. Data for conventional hypersonic vehicles, shown as the open circles, form an almost random "shotgun" pattern which, for the most part, falls below the solid curve.
   (The numbers adjacent to these open circles pertain to specific reference numbers itemized in Ref. 7, which should be consulted for details.)
3. The solid symbols pertain to the present study, and represent a new class of hypersonic configurations which break the "L/D barrier." These configurations are conical flow waveriders that are optimized with detailed viscous effects included directly in the optimization process.

To help understand the contribution made by the present work, let us briefly review the general concept of waveriders. In 1959, the design of three-dimensional hypersonic vehicles which support planar attached shock waves was introduced by Nonweiller,[8,9] who hypothesized that streamsurfaces from the flow behind a planar oblique shock could be used as supersonic lifting surfaces. This led to a class of vehicles with a caret-shaped transverse cross-section and a delta planform-- the so-called caret wing as shown in Fig.4. Here, the body surface is generated by stream surfaces behind a planar oblique shock wave. The shock wave is attached to the sharp leading edges at the design Mach number, and hence no flow spillage takes place around the leading edge. The lift is high due to the high pressures behind a two-dimensional planar shock wave, exerted on the lower surface of the vehicle. Because the body appears to be riding on top of the attached shock wave, it is called a "waverider". The aerodynamic advantages of such waveriders are listed in Ref. 1, and are discussed in great detail in Refs. 7 and 10. In short, without repeating the details here, at a given lift coefficicent, caret waveriders theoretically operate at higher L/D values than other hypersonic configurations.

Expanding on this philosophy, other types of flowfields can be used to generate waveriders. For example, any streamsurface from the supersonic flow over an axisymmetric body can be used to generate a waverider with an attached shock wave along its complete leading edge. Work on such waveriders was first carried out in Britain, as nicely summarized in Ref. 11, where the flow over a right-circular cone at zero degrees angle of attack is used to generate a class of "conical flow" waveriders. Still later, waveriders were generated from inclined circular and elliptic cones, and axisymmetric bodies with longitudinal curvature by Rasmussen et al.[12,13], using hypersonic small disturbance theory. This work was further embelished by the search for optimized waverider shapes. For example Cole and Zien found optimized waveriders derived from axisymmetric bodies with longitudinal curvature by using hypersonic small disturbance theory to generate inviscid flow solutions, and then utilizing the calculus of variations to obtain the optimum waverider shapes. Later, Kim et al. used the same philosophy to derive optimum waveriders from flowfields about unyawed circular cones[15], and yawed circular and elliptic cones[16]. In Refs. 14-16, the advantage of hypersonic small disturbance theory is that analytic expressions are obtained for surface pressure distributions, hence lift and wave drag, thus enabling the application of the calculus of variations for optimization.

Unfortunately, to date the potential superiority of waveriders as hypersonic high L/D shapes has not been fully demonstrated, either in the wind tunnel or in flight. A basic problem arises because of the tendency for waveriders to have large wetted surface areas, which leads to large friction drag. All previous waverider optimization work (such as Refs. 14-16) has been based on the assumption of inviscid flow, after which an estimate of skin friction for the resulting configuration is sometimes added. As a result, the real aerodynamic performance of the resulting optimum configuration usually falls short of its expectations.

The purpose of the present work is to remove this deficiency. In particular, a series of conical-flow generated waveriders are optimized for maximum L/D wherein detailed viscous effects (including boundary layer transition) are included within the optimization process itself. This leads to a new class of waveriders where the optimization process is trying to reduce the wetted surface area, hence reducing skin friction drag, while at the same time maximizing L/D. Because detailed viscous effects can not be couched in simple analytical forms, the formal optimization methods based on the calculus of variations can not be used. Instead, in the present work a numerical optimization technique is used, based on the simplex method by Nelder and Mead[17]. By using a numerical optimization technique, other real configuration aspects can be included in the analysis in addition to viscous effects, such as blunted leading edges, and an expansion upper surface (in contrast to the standard assumption of a free stream upper surface, i.e., an upper surface with all generators parallel to the freestream direction). The results of the present study lead to a new class of waveriders, namely "viscous optimized" waveriders. Moreover, these waveriders appear to produce relatively high values of (L/D), as will be discussed in subsequent sections.

## II. ANALYSIS

For the present waverider configurations, the following philosophy is followed:

1. The lower (compression) surface is generated by a streamsurface behind a conical shock wave. The inviscid conical flowfield is obtained from the numerical solution of the Taylor-Maccoll equation, derived for example in Ref. 18.

2. The upper surface is treated as an expansion surface, generated in a similar manner from the inviscid flow about a tapered, axisymmetric cylinder at zero angle of attack, and calculated by means of the axisymmetric method of characteristics.

3. The viscous effects are calculated by means of an integral boundary layer analysis following surface streamlines, including transition from laminar to turbulent flow.

4. Blunt leading edges are included to the extent of determining the maximum leading edge radius required to yield acceptable leading edge surface temperatures, and then estimating the leading edge drag by modified Newtonian theory.

5. The final waverider configuration, optimized for maximum L/D at a given Mach number and Reynolds number with body fineness ratio as a constraint, is obtained from the numerical simplex method taking into account all the effects itemized in 1-4 above within the optimization process itself.

The following paragraphs describe each of the above items in more depth; for a highly detailed discussion, see Ref. 7.

### A. Inviscid Flow -- Lower Surface

The waverider's lower surface is generated from a streamsurface behind a conical shock wave supported by a hypothetical right circular cone at zero angle of attack. The hypothetical cone and its flowfield is shown in Fig. 5, where $\theta_c$ is the cone semi-angle and $\theta_s$ is the wave angle. The inviscid conical flow is obtained from the Taylor-Maccoll equation[18]

$$\frac{\gamma-1}{2}\left[1-V_r^2-\left(\frac{dV_r}{d\theta}\right)^2\right]\left[2V_r+\frac{dV_r}{d\theta}\cot\theta+\frac{d^2V_r}{d\theta^2}\right] - \frac{dV_r}{d\theta}\left[V'_r\frac{dV_r}{d\theta}+\frac{dV_r}{d\theta}\frac{d^2V_r}{d\theta^2}\right] = 0 \qquad (1)$$

solved by a standard Runge-Kutta, forth-order accurate numerical technique, namely the RKF45 algorithm obtained from Ref. 19. In Eq.(1), $V_r$ is the component of nondimensional flow velocity along a conical ray, $\theta$ is the angle of the ray referred to the cone axis, and $\gamma$ is the ratio of specific heats.

Any streamsurface from this flowfield can represent the wing undersurface of a waverider, as shown in Fig. 6. (For purposes of illustration, Fig. 6 also shows the waverider upper surface as a freestream surface, but this is only one of many possible choices for the upper surface.) Any particular undersurface is uniquely defined by the intersection of the conical flow streamsurface with the conical shock wave, as shown by the curve labeled "leading edge" in Fig. 7. Let us examine Fig.7 more closely. It is a front-view of the hypothetical conical flowfield, illustrating the cone apex at the center, and both the cone base and shock base at some arbitrary distance downstream of the apex. Consider a curve in this front-view, lying below the apex (or even including the apex), as shown by the curve labeled "leading edge". Now construe this curve as a trace on the conical shock wave itself, and visualize streamlines trailing downstream from this trace; the resulting streamsurface is the waverider undersurface sketched in Fig. 6. Indeed, the curve labeled "leading edge" in Fig. 7 is simply the forward projection of the waverider leading edge on the cross-flow (x-y) plane. This curve is treated as completely general, except for the constraints that it be symmetric about the y-z plane, and that it lie entirely below the x-z plane to ensure that the waverider undersurface is a compression surface. Also in Fig. 7, note the curve labeled "trailing edge". This is the intersection of the particular conical flow streamsurface with the plane of the shock base, and it represents the bottom surface trailing edge of the waverider. This is the shape of the bottom of the waverider base, as sketched in Fig. 6. Returning to Fig.7, the area between the "leading edge" and "trailing edge" curves is the forward projection of the entire waverider compression surface. Moreover, the dashed line emanating from the cone apex in Fig. 7 is the forward projection of a conical flow streamline; hence, that portion of the dashed line contained between the "leading edge" and "trailing edge" curves is the projection of a particular streamline along the waverider undersurface, from the leading edge to the trailing edge.

### B. Inviscid Flow -- Upper Surface

In most previous waverider work, the upper surface is treated as a freestream surface, as illustrated in Fig. 6. Here, the upper surface pressure is freestream pressure, $p_\infty$. However, if the upper surface is made an expansion surface, where $p<p_\infty$, then a small but meaningful contribution to L/D can be obtained. This approach is taken here. Similar to the philosophy for the lower surface, the upper surface is a streamsurface "carved" from a known expansion flow. The hypothetical expansion body chosen here is a circular cylinder of given radius; the cyclinder is aligned parallel to the flow and, at some point, is tapered parabolically to a smaller radius. The result is an axisymmetric expansion flow, where the domain of expansion is bounded by a freestream Mach cone centered on the cylinder axis, as shown in Fig. 8. Parabolic taper was chosen because it is relatively simple, and the resulting expansion body slope is everywhere continuous. Once the expansion body is chosen, it remains only to geometrically position the expansion region relative to the lower surface, choose the initial and final cylinder radii, solve the inviscid expansion flow, then cut a streamsurface from that flow to serve as the waverider upper surface. This basic idea was first developed for two-dimensional expansions by Flower[20], and later for axisymmetric expansions by Moore[21].

The axisymmetric flow is calculated from the axisymmetric method of characteristics, using the two-step predictor-corrector iteration scheme of Ferri[22]. The details involving the matching of the resulting expansion surface with the conical flow compression surface are straight forward, but lengthy. Considering that the expansion surface contributes only about 10% to the value of (L/D), no further space for its discussion is justified in the present paper; for the complete discussion, see Ref. 7.

### C. Leading-Edge Bluntness

Waveriders, by design, have sharp leading edges that support attached shock waves. However, for flight Mach numbers above five, the temperatures for sharp leading edges will exceed the practical limits of most structural materials. This leads to the need for blunt leading edges with sufficiently large radii such that the aerodynamic heat flux is reduced to reasonable levels. However, at the same time the leading edge radius should be as small as possible to reduce the nose drag.

To reduce the required leading edge radius, Nonweiler[23] has proposed adding conducting material aft of the leading edge to transport thermal energy away from the region of high convective heating near the stagnation or attachment line, and conduct it downstream to areas where convective heating is lower, and excess energy can be radiated away from the body. Nonweiler labeled this theoretical concept as a "conducting plate", which is somewhat analogous to other passive cooling techniques, such as heat pipes. Using Nonweiler's basic technique, minimum leading edge radii can be ascertained, once flight Mach number, freestream conditions, leading edge sweep, material properties, and maximum allowable temperature are known.

In the present work, Nonweiler's technique was used to determine the leading edge radii for waveriders designed for Mach numbers between 6 and 25. The leading edge material used for the calculations was ATJ graphite, chosen because it is representative of materials with high conductivity and high melting point temperature. Details of this technique as applied to the present work are given in Ref. 7. It is interesting to note that, for conditions associated with the typical flight path of a lifting hypersonic vehicle entering the earth's atmosphere at Mach 25 and decelerating to Mach 6 at lower altitude, the minimum leading edge diameters ranged from 6 to 28 mm -- quite small in comparison to a typical overall length of, say 60m. Therefore, the present waveriders are essentially "aerodynamically sharp" from that point of view. Regardless of the apparently small amount of required leading edge bluntness (from the aerodynamic heating point of view), the present waveriders were geometrically altered to accomodate the blunt edge, and the contribution to aerodynamic forces on the waverider were estimated assuming a modified Newtonian pressure distribution on the leading edge.

### D. Viscous Flow Analysis

A major aspect of the present investigation is that optimum waverider shapes are obtained wherein detailed viscous effects are included within the optimization process itself. These viscous effects are calculated by means of two integral boundary layer techniques, described below. In all cases, the boundary layer flow is assumed to be locally two-dimensional, following the inviscid upper surface and lower surface streamlines. Both laminar and turbulent flow are considered, along with a transition region based on empirical correlations.

#### D.1 Laminar Analysis

The laminar boundary layer calculations were performed using Walz' integral method, as described in Ref. 24. The method requires the solution of a set of coupled first-order ordinary differential equations along the boundary layer edge streamlines. These equations are the boundary layer momentum and mechanical energy equations, given by

Momentum:
$$Z' + \frac{u_e'}{u_e} F_1 Z - F_2 = 0 \qquad (2)$$

Mechanical Energy:
$$W' + \frac{u_e'}{u_e} F_3 W - \frac{F_4}{Z} = 0 \qquad (3)$$

where

$$Z = \delta_2 \left(\frac{\rho_e u_e \delta_2}{\mu_w}\right) \qquad (4)$$

$$W = \delta_3/\delta_2 \qquad (5)$$

$$\delta_1 \equiv \int_0^\delta \left(1 - \frac{\rho u}{\rho_e u_e}\right) dy \qquad (6)$$

$$\delta_2 \equiv \int_0^\delta \frac{\rho u}{\rho_e u_e} \left(1 - \frac{u}{u_e}\right) dy \qquad (7)$$

$$\delta_3 \equiv \int_0^{\delta} \frac{\rho u}{\rho_e u_e}\left(1 - \frac{u^2}{u_e^2}\right)dy \qquad (8)$$

and

$$F_1 = 3+2H-M_e^2+n\,\frac{u_w'/u_w}{u'/u_e}\,,\quad n = \begin{cases} 0, & T_w = \text{constant} \\ 1, & T_w \neq \text{constant}\end{cases} \qquad (9)$$

$$F_2 = 2a/b \qquad (10)$$

$$F_3 = 1-H+r(\gamma-1)M_e^2\left(1-\frac{\tilde{\theta}}{W}\right) \qquad (11)$$

$$F_4 = (2\beta-aW)/b \qquad (12)$$

Note that in the above equations, primes denote differentiation with respect to x, here representing the boundary layer coordinate in the streamline direction. The variables in Eqs. (9)-(12) are defined by Walz to be

$$H = \delta_1/\delta_2 = bH_{12}+r\,\frac{\gamma-1}{2}\,M_e^2(W-\tilde{\theta}) \qquad (13)$$

$$a = 1.7261\ (W^*-1.515)^{0.7158} \qquad (14)$$

$$b = \frac{(\delta_2)_u}{\delta_2} = 1+r\,\frac{\gamma-1}{2}\,M_e^2(W-\tilde{\theta})(2-W) \qquad (15)$$

$$r = \sqrt{Pr} \qquad (16)$$

$$\tilde{\theta} = \frac{T_{aw}(x)-T_w(x)}{T_{aw}(x)-T_e(x)} \qquad (17)$$

and $\beta = \beta_u x$ (18)

where

$$H_{12} = 4.0306 - 4.2845\ (W^*-1.515)^{0.3886} \qquad (19)$$

$$T_{aw} = T_e + \frac{ru_e^2}{2C_p} \qquad (20)$$

$$W^* = (\delta_3)_u/(\delta_2)_u = W/\psi \qquad (21)$$

$$\psi = 1 + \frac{(\psi_{12}-1)M_e}{M_e+\dfrac{\psi_{12}-1}{\psi_o'}} \qquad (22)$$

$$\psi_{12} = \frac{2-(\delta_1)_u/\delta}{W^*}\,\tilde{\theta} + \frac{1-(\delta_1)_u/\delta}{W^*g}\,(1-\tilde{\theta}) \qquad (23)$$

$$\psi_o' = 0.0144(2-W^*)(2-\theta)^{0.8} \qquad (24)$$

$$(\delta_1)_u/\delta = 0.420 - (W^*-1.515)^{0.424W^*} \qquad (25)$$

$$g = 0.324+0.336(W^*-1.515)^{0.555} \qquad (26)$$

$$\beta_u = 0.1564 + 2.1921\ (W^*-1.515)^{1.70} \qquad (27)$$

and

$$\chi = \left\{1+r\left(\frac{\gamma-1}{2}\right)M_e^2\left[1.16W^*-1.072-\tilde{\theta}(2W^*-2.581)\right]\right\}^{0.7}$$

$$\cdot\left[1+r\left(\frac{\gamma-1}{2}\right)M_e^2(1-\tilde{\theta})\right]^{-0.7} \qquad (28)$$

Careful inspection of Eq. (21) reveals that it is an implicit equation for W*, since ψ is a complex function of W*. Therefore, in practice, a numerical zero-finding routine is used on Eq. (21) to find the value of W* that yields the known value of W. Walz suggested an approximation that would allow closed form solution of Eq. (21), however, the present authors have found that it made boundary layer calculations blow up when used for a Mach six flat plate test case. Hence, the suggested approximation was discarded in favor of the zero-finding approach. For more details on the numerical solution of these integral boundary layer equations, see Ref. 7.

### D.2 Turbulent Analysis

If and when boundary layer transition is predicted, turbulent boundary layer calculations are performed using the inner variable integral method of White and Christoph[25]. In practice, the method requires solution of one of two first-order ordinary differential equations along the boundary layer edge streamlines, depending upon the value of the parameter $\lambda/\lambda_{max}$, where

$$\lambda = \sqrt{\frac{2}{C_f}} \qquad (29)$$

$$\lambda_{max} = 8.75\ \log_{10}\ Re^* \qquad (30)$$

$$S = \frac{(T_{aw}/T_e-1)^{1/2}}{\sin^{-1}A+\sin^{-1}B} \qquad (31)$$

$$\text{and}\quad Re^* = \frac{\rho_e}{\mu_w}\left(\frac{T_e}{T_w}\right)^{1/2}\frac{u_e^2}{u_e'} \qquad (32)$$

In Eq. (31), the parameters A and B are defined as

$$A = a/c \qquad (33)$$

$$B = b/c \qquad (34)$$

where

$$a = \frac{T_{aw}+T_w}{T_e} - 2 \qquad (35)$$

$$b = \frac{T_{aw}-T_w}{T_e} \qquad (36)$$

$$c = \left[\left(\frac{T_{aw}+T_w}{T_e}\right)^2 - 4\,\frac{T_w}{T_e}\right]^{1/2} \qquad (37)$$

and Taw is defined by Eq. (20), except that now the recovery factor is the turbulent value,

$$r = Pr^{1/3} \qquad (38)$$

According to Ref. 24, if $\lambda/\lambda_{max} < 0.36$, or $Re^* < 0$, then the differential equation

$$\lambda' = \frac{1}{8}\frac{\rho_e}{\mu_w}\left(\frac{T_e}{T_w}\right)^{1/2} u_e \exp\left(-0.48\frac{\lambda}{S}\right) - 5.5\frac{u_e'}{u_e} \tag{39}$$

is valid; however if $\lambda/\lambda_{max} > 0.36$, then the equation

$$\lambda' = \frac{\frac{-u_e'}{u_e}\left(1 + 9S^{-2}g^* Re^{*0.07}\right)}{0.16 f^* S^3} + \frac{\left[\frac{u_e u_e'' - 2(u_e')^2}{u_e u_e'}\right]\left(3S^2 g^* Re^{*0.07}\right)}{0.16 f^* S^3} \tag{40}$$

applies, where

$$f^* = (2.434z + 1.443z^2)\exp(-44\ z^6) \tag{41}$$

$$g^* = 1 - 2.3z + 1.76z^3 \tag{42}$$

$$z = 1 - \lambda/\lambda_{max} \tag{43}$$

and the primes denote, as in the laminar case, differentiation with respect to the streamline coordinate, x. For more details concerning the numerical solution of these equations, see again Ref. 7.

### D. 3 Transition Analysis

The prediction of transition from laminar to turbulent flow at hypersonic speeds is a state-of-the-art research topic. In the present analysis, the correlation used for predicting the onset of transition is based on two sets of data: (1) data for sharp cones at zero angle-of-attack[26]; and (2) data for wings with blunt, swept supersonic leading edges[27]. The correlation gives local transition Reynolds number $Re_{x_t}$, as a function of local edge Mach number, $M_e$, as follows[26]:

$$\log_{10}(Re_{x_t}) = 6.421 \exp\left(1.209\times10^{-4} M_e^{2.641}\right) \tag{44}$$

In turn, this value of transition Reynolds number is modified for wing leading-edge sweep, as follows[27]:

$$\frac{(Re_{x_t})_\Lambda}{(Re_{x_t})_{\Lambda=0}} = 0.787\cos^{4.346}\Lambda - 0.7221e^{-0.0991\Lambda} + 0.9464 \tag{45}$$

where $\Lambda$ is the sweep angle, and $(Re_{x_t})_{\Lambda=0}$ is obtained from Eq.(44).

Once the onset of transition has been predicted, the extent of the transition region, hence the end of transition, is predicted using a relationship developed by Harris and Blanchard[28], as follows:

$$x_{te} = x_{ti}\left[1 + 5(Re_x)_{ti}^{-0.2}\right] \tag{46}$$

where $x_{te}$ and $x_{ti}$ are the distances along a streamline from the leading edge to the beginning and end of transition, respectively, and $(Re_x)_{ti}$ the local Reynolds number at the beginning of transition obtained in the present analysis from Eq.(45).

The variation of local skin friction coefficient within the transitional region (between $x_{te}$ and $x_{ti}$) is assumed to be a linear combination of the laminar ($c_{f_L}$) and turbulent ($c_{f_T}$) values that would have existed if the boundary layer were completely laminar or turbulent, respectively. The transitional friction coefficient, $c_{f_{TR}}$, is thus related to $c_{f_L}$ and $c_{f_T}$ by:

$$c_{f_{TR}} = (1-\xi)\, c_{f_L} + \xi\, c_{f_T} \tag{47}$$

where $\xi$ is a weighting factor (a function of x) inspired by Emmons (as discussed in Ref.29). For the present investigation, the following expression for $\xi$ is, as derived in detail in Ref. 7:

$$\xi(x) = 1 - e^{-3\left\{\exp\left[\frac{\ln 2}{5x_{ti}}(Re_x)_{ti}^{0.2}(x - x_{ti})\right] - 1\right\}^2} \tag{48}$$

It is not possible within the current state-of-the-art to evaluate the accuracy of these transition correlations. After a study of the existing literature, the present authors feel that the above relations form a practical method for simulating transition within the goals of the present study. They provide a mechanism for assessing the effect of transition on optimum waverider shapes; indeed, as discussed in the results, one series of numerical experiments is conducted wherein the transition location is varied as a parameter.

### E. Aerodynamic Forces

The lift, drag, and hence L/D is calculated from a detailed integration of the local surface pressures and shear stress over the waverider surface. Consistent with wind tunnel practice as well as other literature, base drag is not included in the present results. (For example, all the data shown in Fig. 3 do not include base drag.) This is done to enable a rational comparison with other data. Moreover, at very high Mach number, the base drag becomes a small quantity in comparison to forebody drag. Details on the pressure and shear stress numerical integration can be found in Ref. 7.

### F. Waverider Optimization

Once a specific shape for the forward leading edge projection of a waverider is chosen, (such as shown in Fig. 7), the techniques outlined in the previous sections can be used to generate the corresponding waverider and evaluate its lift-to-drag ratio (L/D). Finding the leading edge shape that maximizes L/D, with all other parameters held fixed, then requires an optimization scheme that can systematically change the projected leading edge shape in search of the one that yields maximum L/D. Unfortunately, most existing optimization schemes require that the function of interest have an analytical description -- a requirement not possible in the present work. There is one scheme, however, a *non-linear simplex* method for function minimization by Nelder and Mead[17], that requires nothing more than the ability to numerically evaluate the function. This scheme has been used in the present work to find optimum waveriders.

In general, the scheme of Ref.17 minimizes a function of $n$ variables by comparing values of the function at $(n+1)$ vertices of a "simplex", then replacing the vertex with the highest function value by another point determined via the logic of the scheme. As a result of the algorithm logic, "the simplex adapts itself to the local landscape [of the function surface], elongating down long inclined planes, changing direction on encountering a valley at an angle, and contracting in the neighborhood of a minimum", according to Ref.17. In this scheme, three operations -- reflection, contraction and expansion -- are used to modify the current simplex in an attempt to replace the vertex having the highest function value with one having a lower value. Each of three operations replace one or more of the $(n+1)$ points $(Po, P_1, \ldots, P_n)$ that define the current simplex in n-dimensional space with new points that yield progressively smaller function values $(f_0, f_1, \ldots, f_n)$ at the new vertex points. A graphic illustration of how the method works is shown in Fig. 9 for a hypothetical function, f, of two variables, $C_1$ and $C_2$. In the figure, a triangle with vertices on the function surface represents a possible simplex. In the optimization process, the triangle (simplex) flip-flops down the function valley, expanding if possible to speed up the process, then contracting when it straddles the minimum.

To use the simplex method for optimizing waverider L/D, the shape of the forward projection of the leading edge must be parameterized in some general way. In the present work, five points in the x-y plane, lying inside of the *shock domain*, were chosen to represent the forward leading edge projection. A cubic spline-fit through the five points is then used to generate a continuous leading edge. One of the five points, the symmetry plane point, is constrained to lie on the y-axis, hence its x- value is always zero. This leaves nine variables, the remaining x and y values of the leading edge projection points, for the optimization routine to manipulate in search of an optimum waverider. A set of leading edge coordinates thus represent a single vertex point,

$$P_i = (x_2, x_3, x_4, x_5, y_1, y_2, y_3, y_4, y_5)_i \qquad (49)$$

of the required simplex, where $x_1 = 0$ as explained, and the function to be minimized is the negative of the lift-to-drag ratio

$$f_i(P_i) = (-L/D)_i \qquad (50)$$

Note that the five leading edge points are used to define only half of the projected leading edge shape, since the other half is constrained by vehicle symmetry to be the mirror image of the first half.

With nine variables (n=9), ten points (hence ten leading edge shapes) must be chosen to create the initial simplex. In the present work, five polynomials of the form

$$y_{\ell e} = C_1 + C_2 x_{\ell e} + C_3 x^2 \qquad (51)$$

$$y_{\ell e} = C_4 + C_5 \cos\left(C_6 \frac{\pi}{2} \frac{x_{\ell e}}{r_s}\right) \qquad (52)$$

were used to describe the initial leading edge shapes; the constants $C_1, C_2, \ldots C_6$ being varied to generate a set of distinct shapes. An example of a set of initial leading edge shapes is shown in Fig. 10 -- the bold line representing the final shape associated with the optimum waverider for this case. Also note that in the present work, 100 steps of the optimization routine were executed for all cases run, though a convergence criterion could have been implemented as described in Ref. 17. It was found that one-hundred steps provided adequate convergence for engineering accuracy ($\sim 10^{-3}$ - $10^{-4}$) without using excessive computer resources to generate an optimized waverider.

For more details on the optimization scheme, see Ref. 7.

## III. RESULTS AND DISCUSSION

The present results are divided into four sections, as follows: (1) a presentation of optimum waverider shapes and aerodynamic characteristics at Mach 6 and 25, representing two extremes of the hypersonic flight spectrum; (2) a numerical experiment to assess the impact of boundary layer transition on the optimized waverider shapes; (3) an assessment of the need to account for detailed surface variations of shear stress in contrast to the use of an average skin friction coefficient during the optimization process; (4) an examination of the question: if the skin friction is deleted from the present analysis, what type of optimized inviscid waverider configuration is produced?

Due to the specialized nature of any waverider generation analysis, including the present one, it is difficult to obtain a direct benchmark comparison with existing data in order to verify the integrity of the current results. However, with the present analysis, it is possible to calculate the aerodynamic properties of a half-cone with a flat delta wing mounted on top; in this case the wing will have a sweep angle corresponding to the shock angle of the cone, and the body will be at zero degrees angle of attack. This specialized case was calculated at Mach 6.8 for a half-cone of $\theta_c = 3.67°$, and the corresponding wing sweep angle of 81°. The result is given as the flagged solid square in Fig.3. This is to be partly compared with the point labeled P2a, which was obtained from Ref. 3, and which corresponds to a similar flat-top half-cone, delta wing model, but at conditions of maximum L/D, hence at some positive angle of attack. About the only point to be made here is that the calculated L/D at zero angle of attack is lower than the measured $(L/D)_{max}$ at some angle-of-attack -- a proper qualitative result. The measured L/D at zero angle-of-attack is not presented in Ref. 3; however, through a personal inquiry to Patrick Johnston at NASA Langley, the present authors have been told that the measured L/D at zero-angle-of-attack was 2.7 -- about eight percent higher than the value of 2.5 calculated with the present analysis. This is a reasonable comparison, and if anything, seems to indicate that the present aerodynamic analysis is conservative. (Please note that the comparisons discussed above are for a given configuration, not an optimized waverider; hence any degree of of validation here pertains to the aerodynamic portion of the analysis and not to the present optimization process itself.)

## A. Representative Waveriders

In Ref. 7, a series of optimized waveriders is generated, including cases at $M_\infty$ = 4,6,10,15,20 and 25. The conditions correspond to altitude-velocity points along a typical entry flight trajectory of a lifting hypersonic vehicle, such as an aerospace plane. In the present section, only the results at $M_\infty$ = 6 and 25 are presented as representative of the two extremes of the flight spectrum. Ref. 7 should be consulted for additional results.

Fig. 11 gives values of (L/D), $C_L$, and volumetric efficiency, $\eta = V^{2/3}/S_p$, for waveriders optimized at different assumed wave angles for the conical shock. To understand this more fully, consider the conical flow field associated with a given conical shock wave, say $\theta_s$ = 11°. For this value of $\theta_s$ an optimum waverider shape is obtained (refer again to the bold curve in Fig. 10). The resulting characteristics of this optimized waverider are then plotted on Fig. 11 for $\theta_s$ = 11°. This process is repeated for other values of $\theta_s$, say 12°, 13°, and 14°. For each value of $\theta_s$, an optimized waverider is obtained, and its characteristics plotted in Fig. 11 as the open symbols. (The solid symbols will be discussed later.) Hence, Fig. 11 pertains to an entire series of optimized waveriders. However, note that the (L/D) curve itself has a maximum (in this case for $\theta_s$ = 12°). This yields an "optimum of the optimums", and defines the final viscous optimized waverider at $M_\infty$ = 6 for the flight conditions shown in Fig. 11. The front views of the optimum shapes at each value of $\theta_s$ are shown in Fig. 12, and the corresponding perspective views are shown in Fig. 13. Finally, a summary three-view of the best optimum (the "optimum of the optimum") waverider, which here corresponds to $\theta_s$ = 12°, is given in Fig. 14. Also in Figs. 12-14, the lines on the upper and lower surfaces of the waveriders are inviscid streamlines. Note in these figures that the shape of the optimum waverider changes considerably with $\theta_s$. Moreover, examining (for example) Figure 14, note the rather complex curvature of the leading edge in both the planform and front views; the optimization program is shaping the waverider to adjust both wave drag and skin friction drag so that the overall L/D is a maximum. Indeed, it was observed in all of the present results that the best optimum shape at any given $M_\infty$ results in the magnitudes of wave drag and skin friction drag being approximately the same, never differing by more than a factor of two. For conical shock angles below the best optimum (for example $\theta_s$ = 11° in Figs. 12 and 13), skin friction drag is greater than wave drag; in contrast, for conical shock angles above the best optimum (for example $\theta_s$ = 13° and 14° in Figures 12 and 13), skin friction drag is less than wave drag. (Note: For a hypersonic flat plate, using Newtonian theory and an average skin friction coefficient , it can readily be shown that at maximumum L/D, the wave drag is twice the friction drag.)

The results in Figs. 11-14 pertain to $M_\infty$ = 6. An analogous set of results for the other extreme of the lifting hypersonic flight spectrum at $M_\infty$ = 25 is given in Figs. 15-18. The aerodynamic characteristics of optimum waveriders for $\theta_s$ = 7°,8°,9° and 10° are given as the open symbols Fig. 15 (the solid symbols will be discussed later.) The respective front views are shown in Fig. 16, and perspective views in Fig. 17. Finally, the best optimum Mach 25 waverider (which occurs at $\theta_s$ = 9°) is summarized in Fig. 18. Comparing the optimum configuration at $M_\infty$ = 6 (Fig. 14) with the optimum configuration at Mach 25 (Fig. 18), note that the Mach 25 shape has more wing sweep, and pertains to a conical flowfield with a smaller wave angle, both of which are intuitively expected at higher Mach number. However, note from the flight conditions listed in Figs. 11 and 15 that the body slenderness ratio at $M_\infty$ = 6 is constrained to be $b/\ell$ = 0.06 (analogous to a supersonic transport such as the Concorde) but that $b/\ell$ = 0.09 is the constraint chosen at $M_\infty$ = 25 (analogous to a hydrogen fueled hypersonic aeroplane such as the British HOTOL). The two different slenderness ratios are chosen on the basis of reality for two different aircraft with two different missions at either extreme of the hypersonic flight spectrum. Also note in Figs. 16-18 the optimization program has sculptured a best optimized configuration with a spline down the center of the upper surface--an interesting and curious result, due principally to the competing effects of minimizing pressure and skin friction drag, while meeting the slenderness ratio constraint.

Return to Fig. 15, and note the solid symbols. These pertain to the values of $C_L$ and L/D obtained by setting the ratio of specific heats $\gamma$ to 1.1 in order to assess possible effects of high temperature chemically reacting flow. The solid symbols pertain to an optimized waverider at $\theta_s$ = 9° with $\gamma$ = 1.1. This is not necessarily the best optimum at Mach 25 with $\gamma$ = 1.1; rather, it is just a point calculation to indicate that high temperature effects will most likely have a significant impact on optimized waverider generation, and that such effects are worthy of future investigation. The detailed aspects of high temperature effects are beyond the scope of the present paper; additional discussion is given in Ref. 7.

As a final note in this section, return to Fig. 3, and note that the solid symbols pertain to the present investigation. The flagged square has been discussed earlier as the data point for a half-cone with a delta wing at zero angle-of-attack; it is not part of the present waverider family. The unflagged solid square at $M_\infty$ = 4 pertains to a relatively large slenderness ratio of 0.087, used to generate a waverider for wind tunnel testing. The remaining solid symbols, the circles and triangles, pertain to the present discussion. Recall that the circles are for $b/\ell$ = 0.06 (a Concorde-like slenderness ratio for a low Mach number configuration), and that the triangles are for $b/\ell$ =0.09 (a HOTOL-like slenderness ratio for a high Mach number configuration). In the present section, we have discussed results obtained at Mach 6 and 25; Fig. 3 shows these plus others at intermediate Mach numbers. All of these cases are discussed in detail in Ref. 7. However, in regard to Fig.3, emphasis is now made that the present viscous optimized waveriders produce values of (L/D) which exceed the "L/D barrier" discussed in Section I, and shown as the solid curve in Fig.3. Indeed, the present waverider L/D variation is more closely given by

$$(L/D)_{max} = \frac{6(M+2)}{M}$$

shown as the dashed curve in Fig. 3. Note that the two points given for $M_\infty = 20$ and 25 deviate away from the dashed curve. This is a Reynolds number effect. Recall that all the Mach number-altitude points for the present waveriders are chosen to follow a typical lifting vehicle flight path through the atmosphere. The point at Mach 25 is at very high altitude (250,000 ft.), with a corresponding low Reynolds number ($Re = 1.4x10^6$); the flow is completely laminar. At Mach 20, the Reynolds number is 12 times higher, but based on the transition criterion discussed in Section II the flow is still completely laminar. Hence, the laminar skin-friction coefficient at the Mach 20 point in Fig. 3 is much lower ($c_f \propto 1/\sqrt{Re}$) than at the Mach 25 point, with an attendant larger (L/D) at Mach 20. In contrast, the point at Mach 15 is transitional, with regions of both laminar and turbulent flow, and hence with larger skin-friction and a lower (L/D). In any event, the results given in Fig. 3 indicate that the present viscous optimized waveriders produce high values of (L/D), and therefore are worthy of additional consideration for hypersonic vehicle application.

### B. Sensitivity to Transition

Because the major thrust of the present work is the inclusion of detailed viscous effects in the waverider optimization, the question naturally arises: How sensitive are the present waveriders to uncertainties in the location of transition from laminar to turbulent flow? To address this question, a numerical experiment is carried out wherein the transition location was varied over a wide latitude, ranging from all laminar flow on one hand, to almost all turbulent flow on the other hand, with various cases inbetween. Specific results at Mach 10 are given in Fig. 19; here values of (L/D) are given for optimized waveriders as a function of assumed transition location. The point corresponding to the transition correlation described in Section II, D.3, is denoted by "x" in Fig. 19. Other points in Fig. 19 labeled 5x, 10x and 15x correspond to transition locations that are 5, 10 and 15 times the value predicted by the transition correlation. All the data given in Fig. 19 pertain to optimized waveriders for $\theta_s = 9°$, which yields the best optimum at Mach 10 for the usual transition correlation. (Note, however, that $\theta_s = 9°$ may not yield the best optimum for other transition locations; this effect is not investigated here.) The results in Fig. 19 demonstrate a major increase in (L/D) in going from almost all turbulent flow to all laminar flow. However, for the case where transition is changed by a factor of five, only a 2% change in L/D results. Even for the case where transition is changed by a factor of ten, a relatively small change in L/D of 11% results. On the other hand, the shapes of the resulting optimized waveriders are fairly sensitive to the transition location, as illustrated in Figs. 20 and 21. The conclusion to be made here is that waverider optimization is indeed relatively sensitive to transition location, and this underscores the need for reliable predictions of transition at hypersonic speeds.

### C. On the Use of Average Skin Friction Coefficients

The present detailed viscous analysis computes the surface shear stress distributions, and integrates over the surface to obtain the total skin friction drag. This requires a substantial amount of computer calculations, and leads to the question: Can an overall average skin friction coefficient be used within the optimization process rather than dealing with the detailed shear stess distributions? To address this question, consider the best optimum Mach six case given in Fig. 11, which was orginally calculated with the detailed shear stress distributions. From this result, an average skin friction drag coefficient was calculated for the complete configuration. Then the optimization code was run again for the same Mach six case, now using this average skin friction drag coefficient. The results are given in Fig. 11 as the solid symbols. Only a small difference exists between the two cases; indeed, the resulting waverider shapes are virtually the same, as given in Ref. 7. This implies that if an accurate average skin friction drag coefficient can be obtained, the resulting optimized waveriders would be reasonably valid. However, the problem with this method is that the information needed to obtain the average skin friction drag coefficient is not known apriori. Moreover, if other independent means are used to obtain an approximate average skin friction drag coefficient and this approximate average value is used in the optimization process, the results can be quite different from those obtained from the use of detailed shear stress distributions; see Ref. 7 for more discussion on this aspect. This situation, in combination with the sensitivity to transition demonstrated in the previous section, seems to dictate the necessity of using the detailed shear stress distributions rather than some approximate average value of skin friction drag coefficient for obtaining the proper optimized waveriders.

### D. Inviscid Optimized Waveriders

As a final note, it is interesting to pose the question: if the skin friction is deleted from the present analysis, what type of optimized inviscid waverider configuration, with a constraint on slenderness ratio, is produced? To examine this question, the present computer code was run without skin friction as part of the optimization process, covering the range of Mach number from 6 to 25. A typical result for the inviscid optimized configuration is shown in Fig.22. Here we see essentially a wedge-like caret waverider, such as the classic configuration generated by the two-dimensional flow behind a planar oblique shock wave, as discussed by Nonweiler[8,9]. This clearly indicates that the optimized inviscid waverider with slenderness ratio as the constraint is indeed a caret wing. The result shown in Fig. 22 is produced by the present conical flow analysis as a "limiting case", wherein the optimum shape is seeking the flattest portion of the conical shock wave. To see this more clearly, return to Fig. 6. The resulting inviscid waveriders are being generated by relatively flat streamsurfaces at the extreme back and bottom of the generating conical flow-field -- where the shock radius of curvature is the largest and the flow is closest to being two-dimensional. Consequently, the inviscid configurations are tiny shapes compared to the scale of the flowfield in Fig. 6, and they are "squeezed" into a tiny area at the bottom of the shock base. In turn, due to the logic of the existing conical flow code, only a few pressure and shear stress points are calculated on the surface of these tiny waveriders, raising questions about the numerical accuracy of the calculation of their lift and drag. Therefore, no further discussion about the inviscid optimized waveriders will be given here, except to emphasize again that a two-dimensional caret wing seems to be the optimum inviscid shape that is predicted by the present conical flow analysis.

## IV CONCLUSIONS

In comparison to previous optimized waverider analyses, the present work is the first to include detailed viscous effects within the optimization process. From this work, the following major conclusions are made:

1. The resulting family of viscous hypersonic waveriders yields predicted high values of $(L/_D)$ which break the "L/D barrier" discussed in Section I.
2. The optimization process for the viscous waveriders results in distinctly different shapes compared to previous work with inviscid-designed waveriders.
3. The fine details of the viscous solution, such as how the shear stress is distributed over the surface, and the location of transition, are crucial to the details of the resulting waverider geometry.

## V. ACKNOWLEDGEMENT

This work was supported through the Graduate Hypersonic Aerodynamics Fellowship Program, established in 1983 at the University of Maryland by the Army Research Office, with Dr. Robert Singleton as monitor. The authors also acknowledge a close working relationship with the Fundamental Aerodynamics Branch at the NASA Langley Research Center under a grant monitered by Wallace Sawyer and Patrick Johnston.

## REFERENCES

1. Anderson, John D. Jr., "A Survey of Modern Research in Hypersonic Aerodynamics," AIAA Paper No. 84-1578. Invited paper given at the AIAA 17th Fluid Dynamics, Plasma Dynamics, and Lasers Conference, Snowmass, Colorado, June 25-27, 1984.

2. Anderson, John D., Jr., "Hypersonic Aerodynamics," notes printed by the AIAA for the Short Course presented in Atlanta, Georgia, May 10-11, 1986.

3. Fetterman, D.E., Henderson, A., Jr., Bertram, M.H., and Johnston, P.J., "Studies Related to the Attainment of High Lift-Drag Ratios at Hypersonic Speeds," NASA TN D-2956, August 1965.

4. Penland, J.A., Marcum, D.C., Jr., and Stack, S.H., "Wall-Temperature Effects on the Aerodynamics of a Hydrogen-Fueled Transport Concept in Mach 8 Blowdown and Shock Tunnels," NASA TP 2159, July 1983.

5. Loftin, Laurence, Quest for Performance; The Evolution of Modern Aircraft, Pergamon Press, Oxford, 1978, pp. 448-510.

6. Kuchemann, D., The Aerodynamic Design of Aircraft, Pergamon Press, Oxford, 1978, pp.448-510.

7. Bowcutt, Kevin G., Optimization of Hypersonic Waveriders Derived from Cone Flows -- Including Viscous Effects, Ph.D. Dissertation, Dept. of Aerospace Engineering, University of Maryland, College Park, Maryland, 1986.

8. Nonweiler, T.R.F., "Aerodynamic Problems of Manned Space Vehicles," Journal of the Royal Aeronautical Society, Vol. 63, 1959, pp. 521-528.

9. Nonweiler, T., "Delta Wings of Shapes Amenable to Exact Shock-Wave Theory," Journal of the Royal Aeronautical Society, Vol. 67, Jan. 1963, pp.39-40.

10. Townend, L.H., "Research and Design for Lifting Reentry," Progress in Aerospace Sciences, Vo. 18, 1979, pp. 1-80.

11. Jones, J.G., Moore, K.C., Pike, J., and Roe, P.L., "A Method for Designing Lifting Configurations for High Supersonic Speeds, Using Axisymmetric Flow Fields," Ingenieur-Archiv, Vol. 37, 1968, pp.56-72.

12. Rasmussen, M.L., "Waverider Configurations Derived from Inclined Circular and Elliptic Cones," J. of Spacecraft and Rockets, Vol. 17, No.6, Nov.-Dec., 1980, pp. 537-545.

13. Rasmussen, M.L., and Clement, L.W., "Cone-Derived Waveriders With Longitudinal Curvature," AIAA Paper No. 84-2100, 1984.

14. Cole, J.D. and Zien, T.F., "A Class of Three-Dimensional, Optimum Hypersonic Wings," AIAA Journal, Vol. 7, No. 2, Feb. 1969, pp.264-271.

15. Kim, B.S., Rasmussen, M.L. and Jischke, M.C., "Optimization of Waverider Configurations Generated from Axisymmetric Conical Flows," AIAA Paper No. 82-1299, 1982.

16. Kim, B.S., Optimization of Waverider Configurations Generated from Non-Axisymmetric Flows Past a Nearly Circular Cone, Ph.D. Dissertation, School of Aerospace, Mechanical, and Nuclear Engr., Univ. of Oklahoma, 1983.

17. Nelder, J.A. and Mead, R., "A Simplex Method for Function Minimization," Computer Journal, Vol.7, Jan. 1965, pp. 308-313.

18. Anderson, John D., Jr., Modern Compressible Flow: With Historical Perspective, McGraw-Hill, New York, 1982.

19. Forsythe, G.E., Malcom, M.A. and Moler C.B., Computer Methods for Mathematical Computations, Prentice-Hall, Inc., New Jersey, 1977.

20. Flower, J.W., "Configurations for High Supersonic Speeds Derived from Simple Shock Waves and Expansions," Journal of the Royal Aeronautical Society, Vol. 67, 1963, p. 287.

21. Moore, K.C., "The Application of Known Flow Fields to the Design of Wings with Lifting Upper Surfaces at High Supersonic Speeds," R.A.E. Tech. Rept. No. 65034, ARC 26913, Feb. 1965.

22. Ferri, A., General Theory of High Speed Aerodynamics, Princeton Series, Sears, W.R. (Editor), Vol. 6, 1954, pp.616-623.

23. Nonweiler, T., Wong, H.Y., and Aggarwal, S.R., "The Role of Heat Conduction in Leading Edge Heating," Ingenieur-Archiv, Vol. 40, 1971, pp. 107-117.

24. Walz, A., Boundary Layers of Flow and Temperature, M. I. T. Press, Cambridge, Mass., 1969.

25. White, F.M., Viscous Fluid Flow, McGraw-Hill, New York, 1974, pp. 653-657.

26. DiCristina, V., "Three-Dimensional Laminar Boundary-Layer Transition on a Sharp 8° Cone at Mach 10", AIAA Journal, Vol. 8, No. 5, May 1970, p. 855.

27. Pate, S.R., and Groth, E.E., "Boundary-Layer Transition Measurements on Swept Wings with Supersonic Leading Edges," AIAA Journal, Vol.4, No.4, April 1966, pp. 737-738.

28. Harris, J.E., and Blanchard, D.K., "Computer Program for Solving Laminar, Transitional, and Turbulent Compressible Boundary Layer Equations for Two Dimensional and Axisymmetric Flows," NASA TM 83207, Feb. 1982.

29. Christoph, G. H., "Law-of-the-Wall Analysis Revisited for Reentry Vehicle Design," AIAA Paper 85-0905, June 1985.

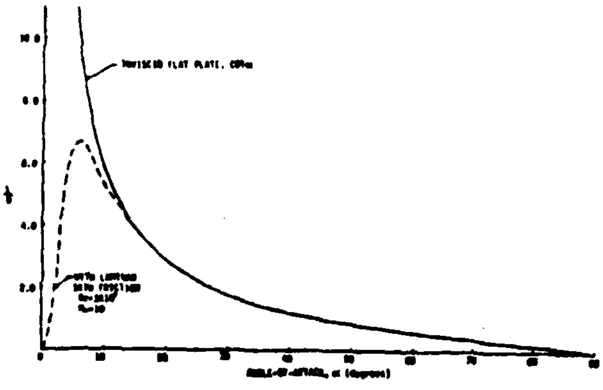

FIG 1: Newtonian results for a flat plate.

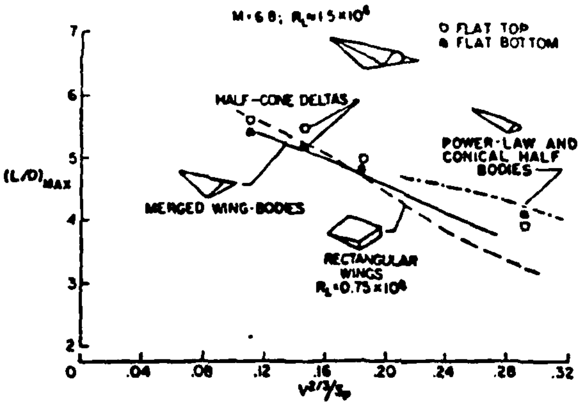

FIG. 2: Performance comparison of various generic hypersonic configurations ( from Ref. 3).

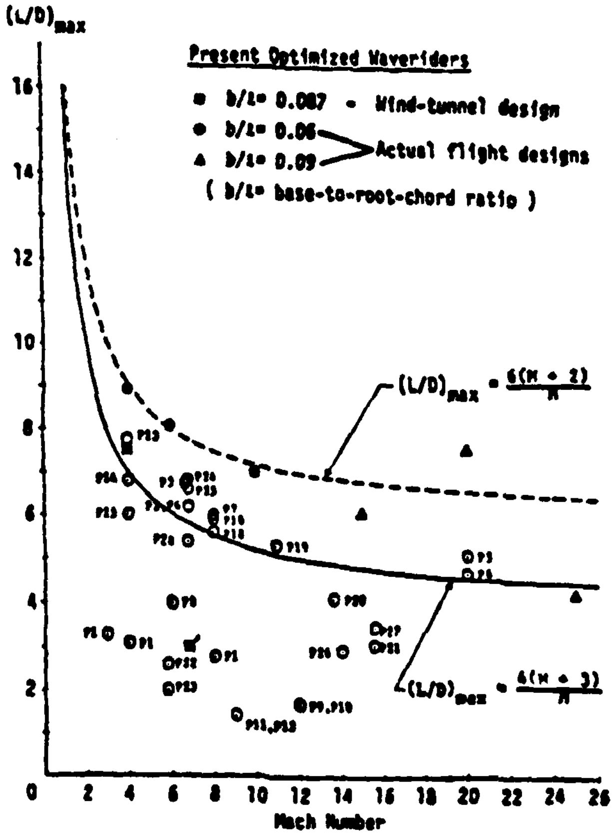

FIG 3: Maximum lift-to-drag ratio comparison for various hypersonic configurations.

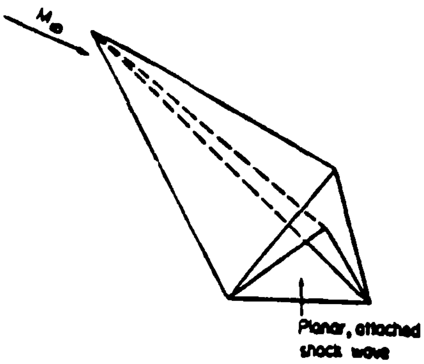

FIG 4: Schematic of a simple caret wing waverider.

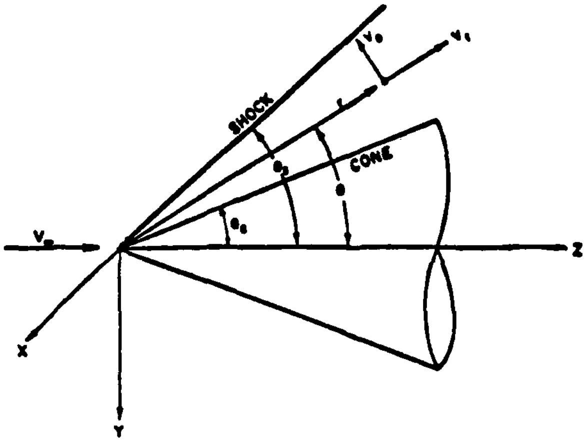

FIG. 5: Spherical coordinate system for cone flow calculations, and cartesian coordinate system for waverider design.

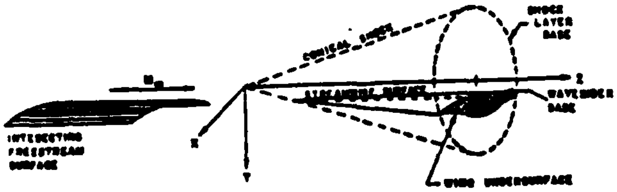

FIG 6: Perspective view of a conical waverider and generating shock.

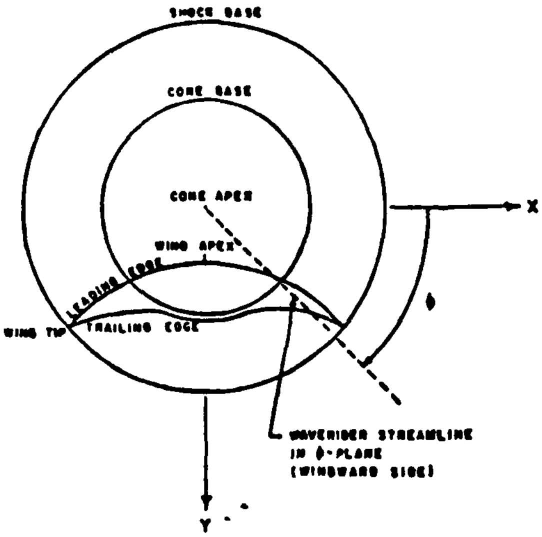

FIG. 7: Front view of a conical waverider with the generating cone and shock.

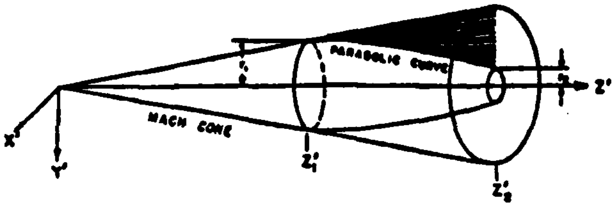

FIG 8: Expansion cylinder and expansion domain bounded by the Mach cone.

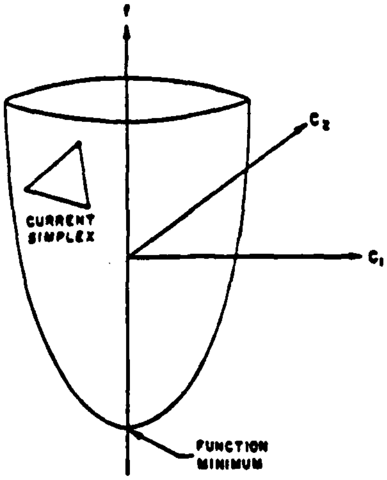

FIG. 9: Example of the optimization process for a function of two variables.

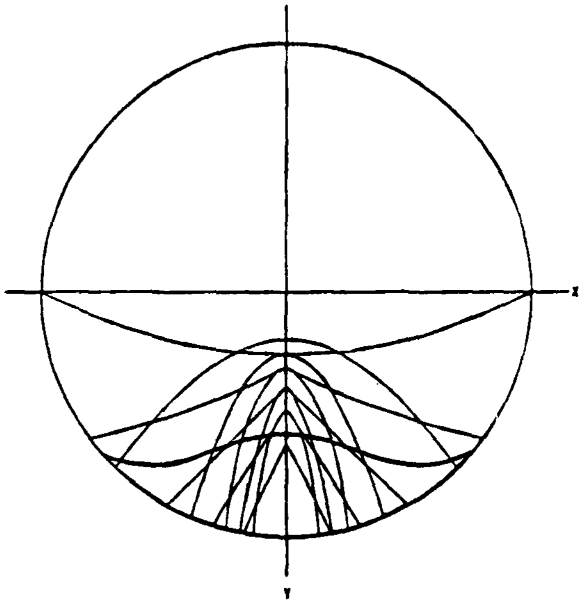

FIG. 10: Example of initial and optimized waverider leading edge shapes.

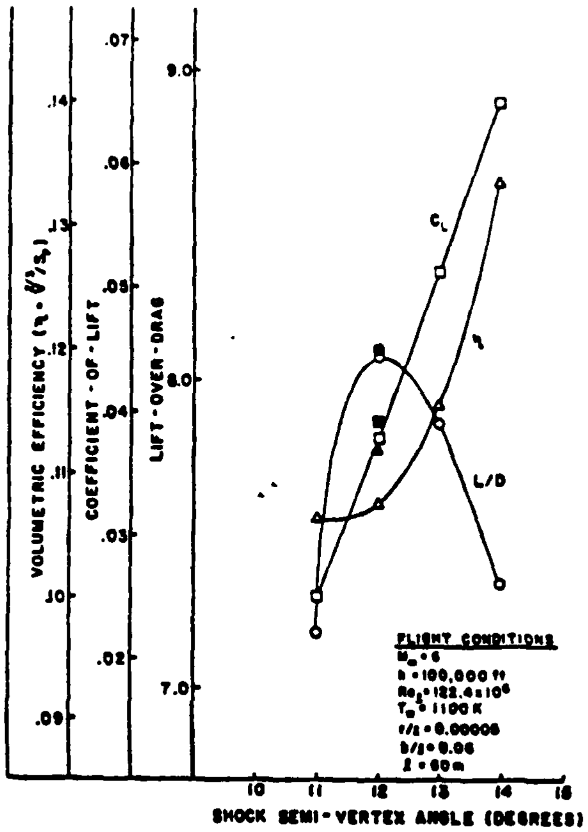

FIG. 11: Results for a series of optimized waveriders at Mach 6.

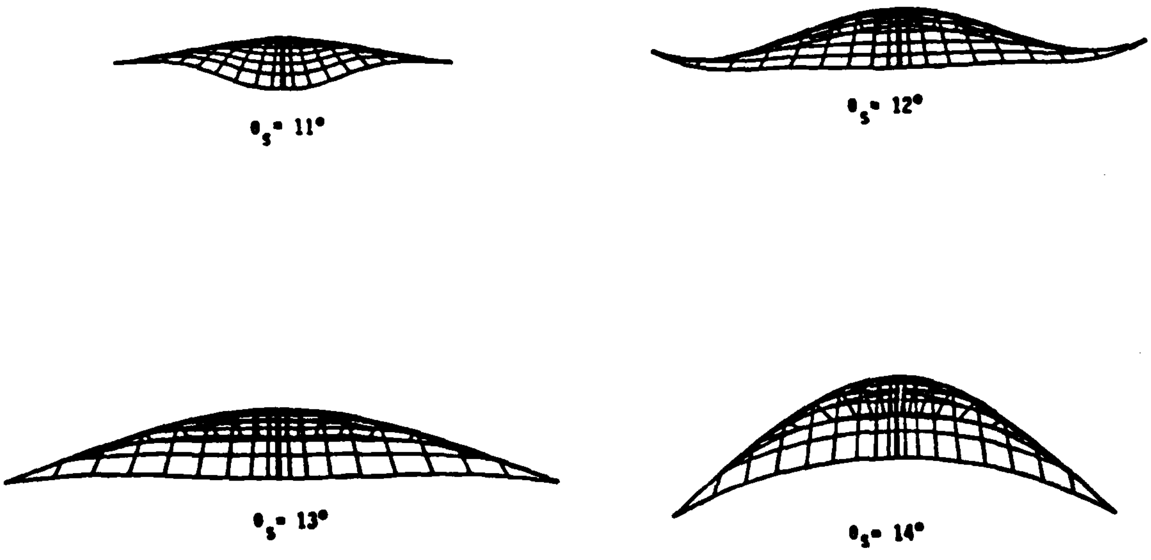

$\theta_s = 11°$

$\theta_s = 12°$

$\theta_s = 13°$

$\theta_s = 14°$

FIG 12: Front views of a series of optimized waveriders at Mach 6.

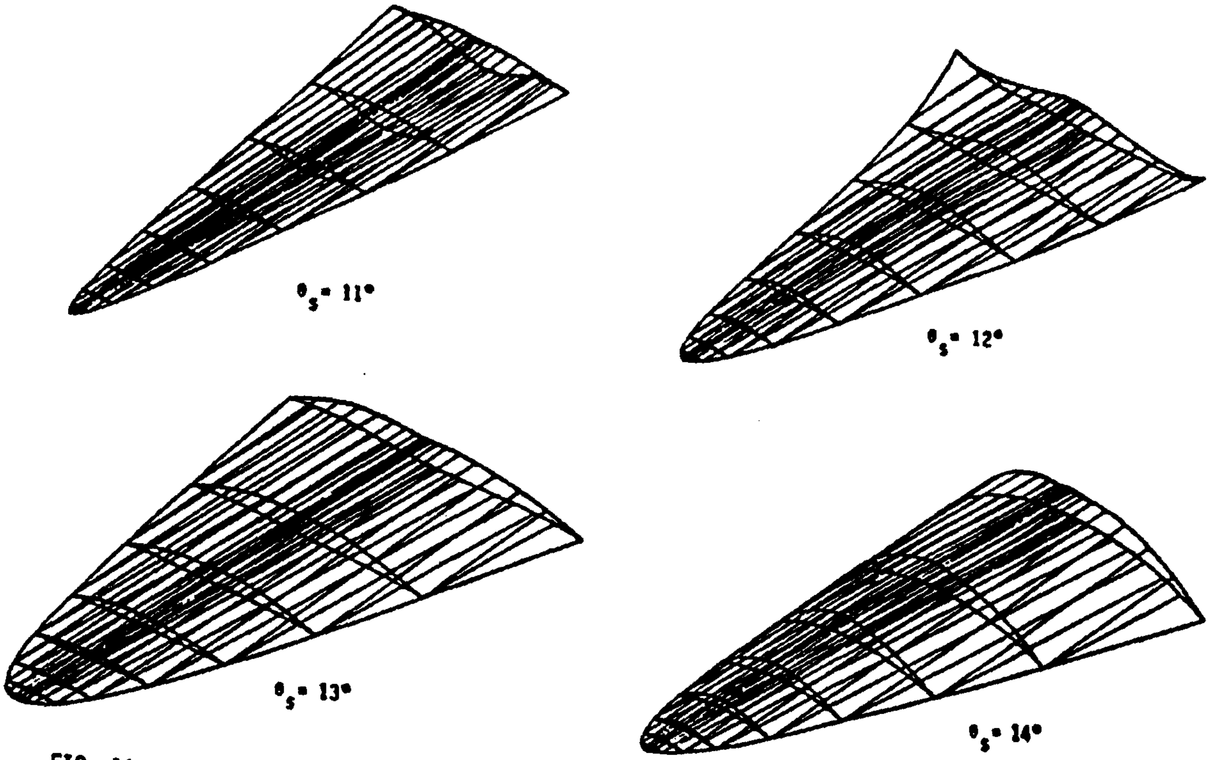

$\theta_s = 11°$

$\theta_s = 12°$

$\theta_s = 13°$

$\theta_s = 14°$

FIG. 13: Perspective views of a series of optimized waveriders at Mach 6.

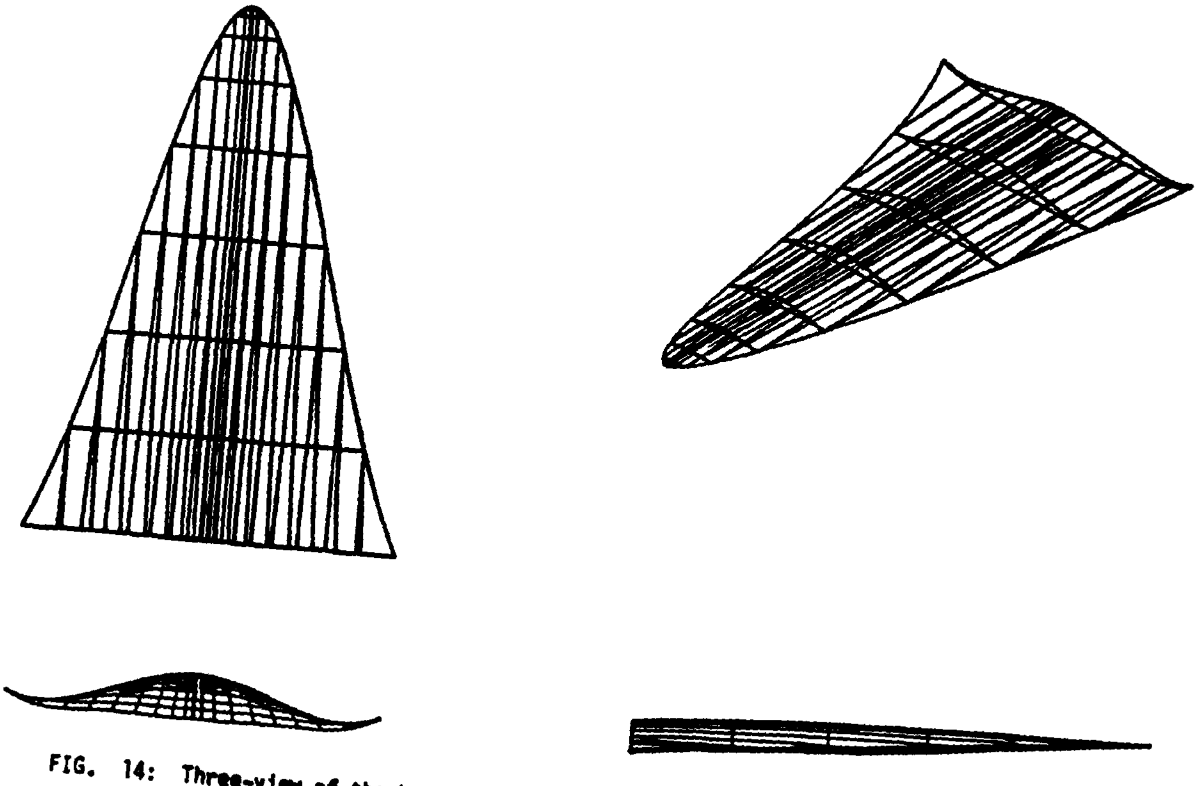

FIG. 14: Three-view of the best optimum waverider at Mach 6. ($\theta_s = 12^{\circ}$)

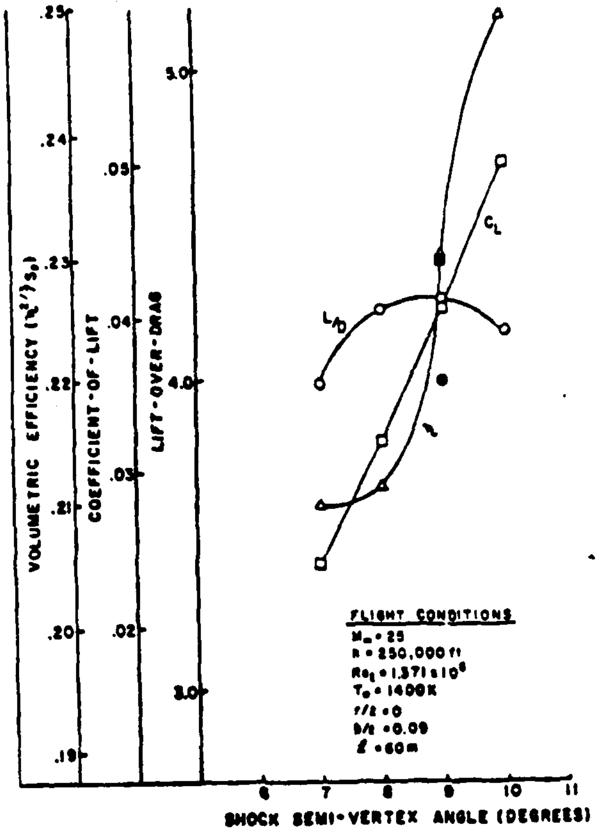

FIG. 15: Results for a series of optimized waveriders at Mach 25.

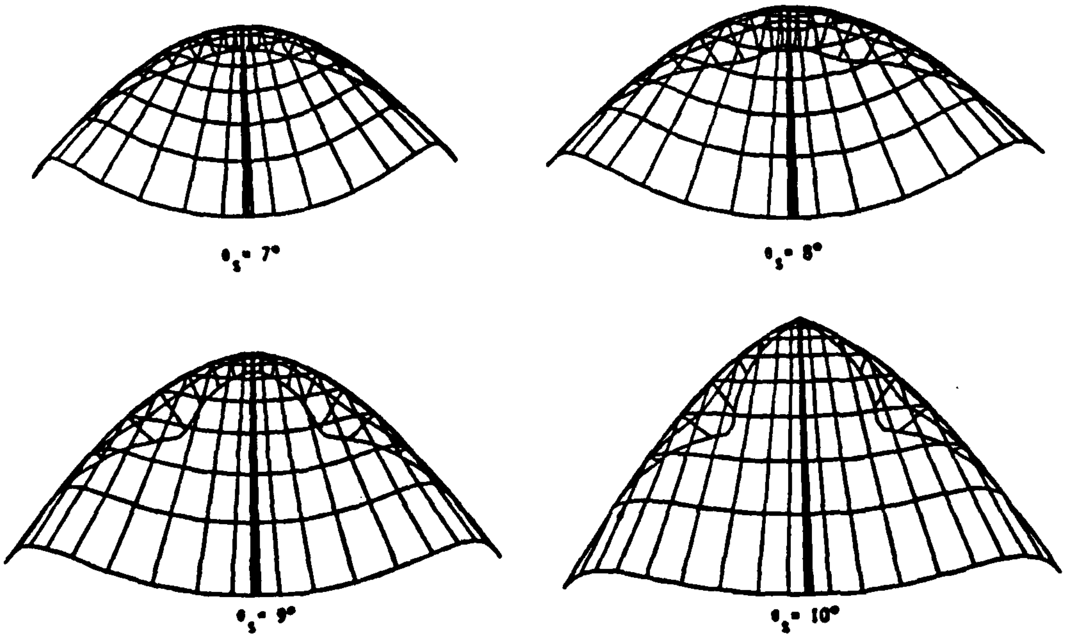
$\theta_s = 7°$

$\theta_s = 8°$

$\theta_s = 9°$

$\theta_s = 10°$

FIG. 16: Front views of a series of optimized waveriders at Mach 25.

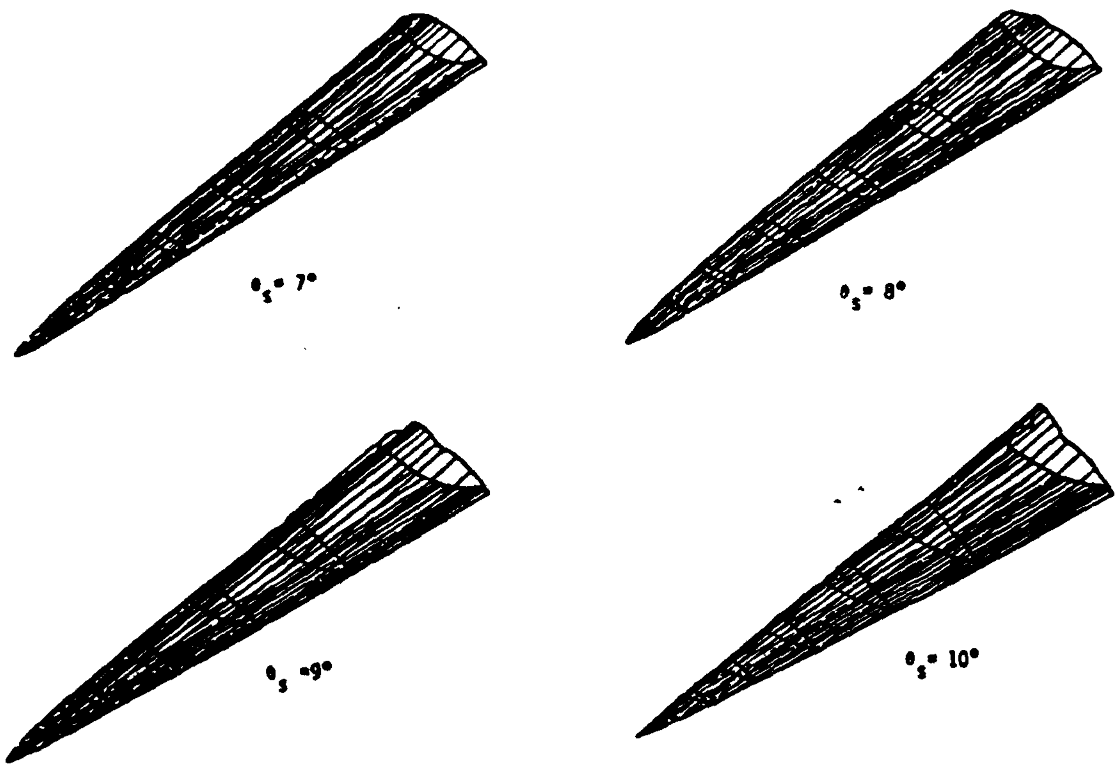

FIG. 17: Perspective views of a series of optimized waveriders at Mach 25.

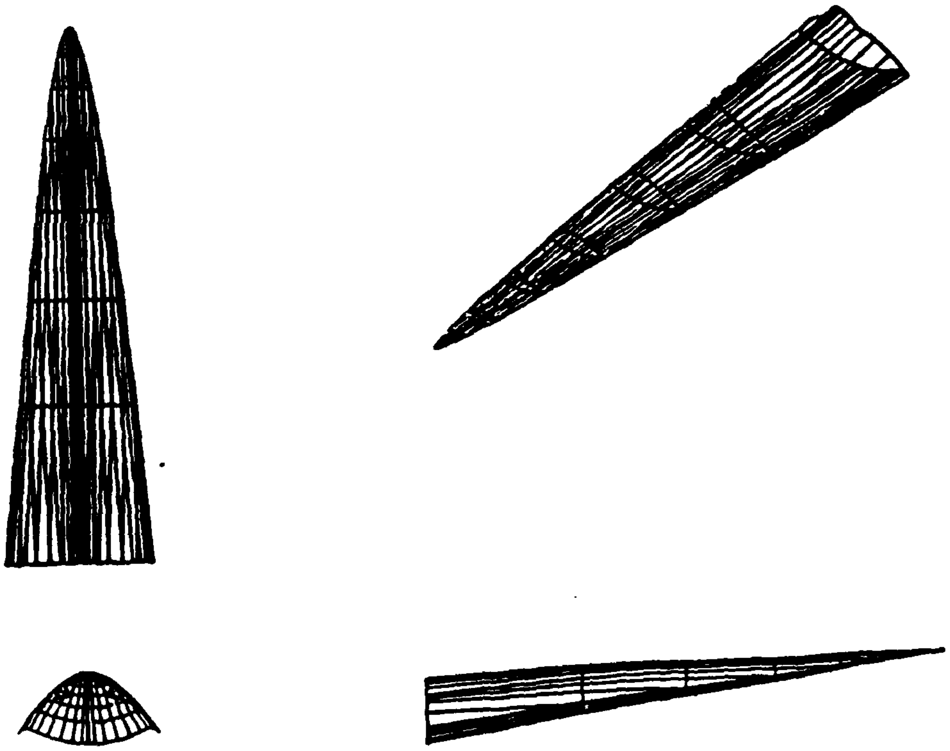

FIG. 18: Three-view of the best optimum waverider at Mach 25. ($\theta_s$ = 9$^0$)

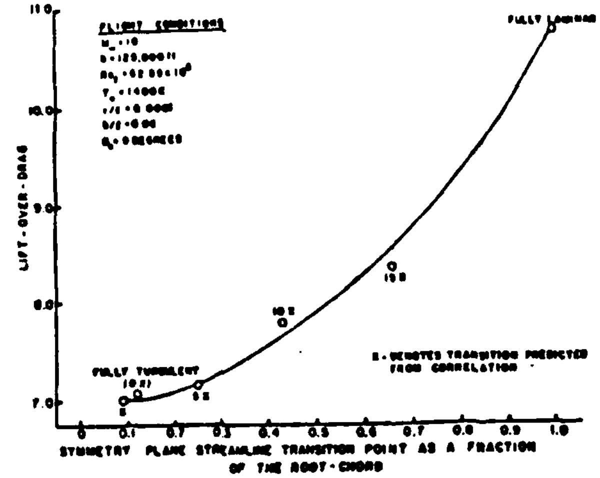

FIG. 19: Lift-to-drag comparison of optimized Mach 10 waveriders designed with various boundary layer transition criteria.

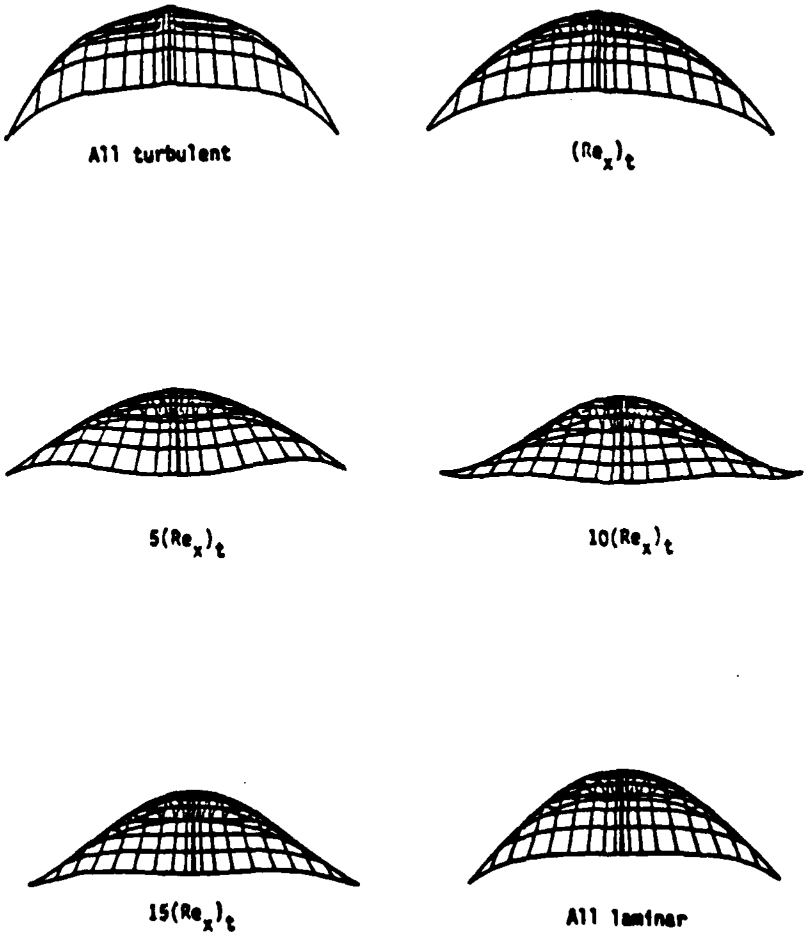

All turbulent

$(Re_x)_t$

$5(Re_x)_t$

$10(Re_x)_t$

$15(Re_x)_t$

All laminar

FIG. 20: Front views of optimized Mach 10 waveriders designed with various boundary layer transition criteria.

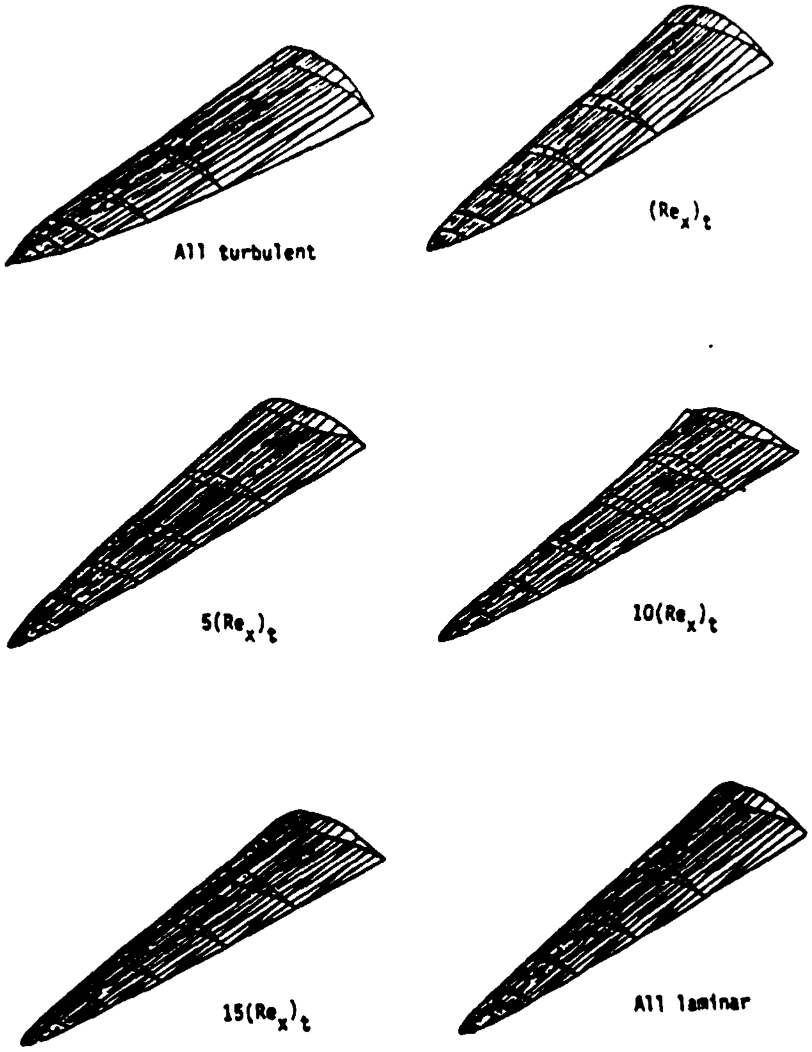
All turbulent

$(Re_x)_t$

$5(Re_x)_t$

$10(Re_x)_t$

$15(Re_x)_t$

All laminar

FIG. 21: Perspective views of optimized Mach 10 waveriders designed with various boundary layer transition criteria.

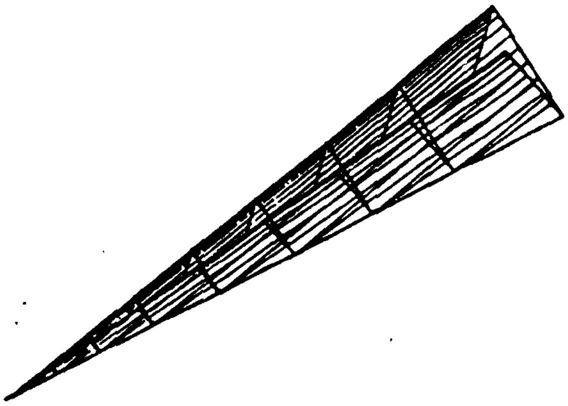

FIG. 22: An optimized inviscid waverider at Mach 10; a caret wing.

# APPENDIX B

AIAA'89

# AIAA 89-0674
# Numerical Solutions to Three-Dimensional Shock Wave/Vortex Interaction at Hypersonic Speeds

G. Copening, Johns Hopkins Univ.,
Laurel, MD;
J. Anderson, Univ. of Maryland,
College Park, MD

## 27th Aerospace Sciences Meeting

January 9-12, 1989/Reno, Nevada

For permission to copy or republish, contact the American Institute of Aeronautics and Astronautics
370 L'Enfant Promenade, S.W., Washington, D.C. 20024

# NUMERICAL SOLUTIONS TO THREE-DIMENSIONAL SHOCK WAVE/ VORTEX INTERACTION AT HYPERSONIC SPEEDS

**AIAA-89-0674**

Griffin Corpening*
The Johns Hopkins University Applied Physics Laboratory
Johns Hopkins Road
Laurel, Maryland 20707

John D. Anderson, Jr.**
Department of Aerospace Engineering
University of Maryland
College Park, Maryland 20742

## Abstract

An upwind difference, finite volume algorithm was used to numerically solve the full three-dimensional Euler equations for two flowfields, Mach numbers 2.28 and 5.00, each containing a helical-type vortex impinging on an oblique shock wave. These solutions showed several interesting and unexpected results. In neither case did the jump across the shock cause the vortices to breakdown. However, two ususual structures were observed. The first was common to both flowfields and was seen as areas of flow reversal around the outside of the post-shock vortex. The second unexpected structure was observed only in the Mach 5.00 flowfield and was seen as the formation of a trough-like structure around the outside of the post-shock vortex. Further study is needed to determine the cause of these structures. They may possibly be a result of vorticity generation due to the nonuniform pre-shock flowfield combined with the shock curvature. To the best of the author's knowledge, this is the first time these two structures have been observed.

## Introduction

A recent study at the University of Maryland has been undertaken to numerically solve the interaction flowfield between a 3-D, helical-type vortex and an oblique shock wave. This paper is based on the work presented in Reference 1. The study investigates Euler solutions to three-dimensional shock wave/ vortex interaction (SW/VI) at two Mach numbers, namely Mach 2.28 and 5.00. Figure 1 shows a schematic of the flowfield. This is the first work known to the authors in which this flowfield has been studied.†

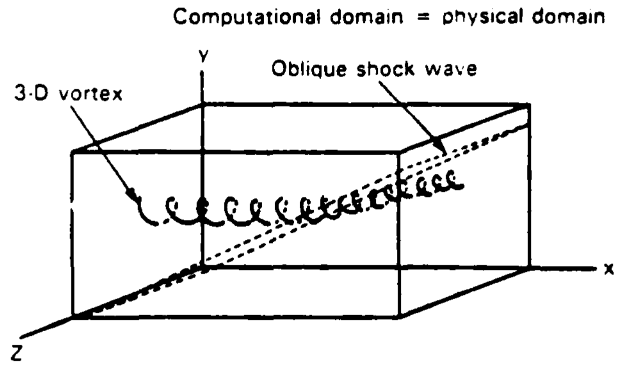

Fig. 1 Schematic of the flowfield.

The study is made up of three parts. In the first part, a numerical model is chosen which is capable of simulating the flowfield. In the second part, an input vortex is developed which can be fed into the upstream boundary of the computational domain. These two parts are then brought together in the third part of the study where the numerical algorithm is used to solve the shock wave/vortex interaction flowfield. Each of these parts are discussed in detail below.

As mentioned above, there has been no work studying this particular interaction problem, although Delery et al in Reference 2 have studied the interaction between an normal shock wave and a vortex. They experimentally investigated the structure of a helical-type vortex in a supersonic flow and studied vortex breakdown†† induced by a normal shock wave. They also developed an inviscid numerical model to simulate the results. Delery et al chose to characterize the vortex by two parameters, the freestream Mach number and the ratio of the maximum tangential velocity divided by the freestream axial velocity. Figure 2 shows the breakdown process as a function of these two parameters.

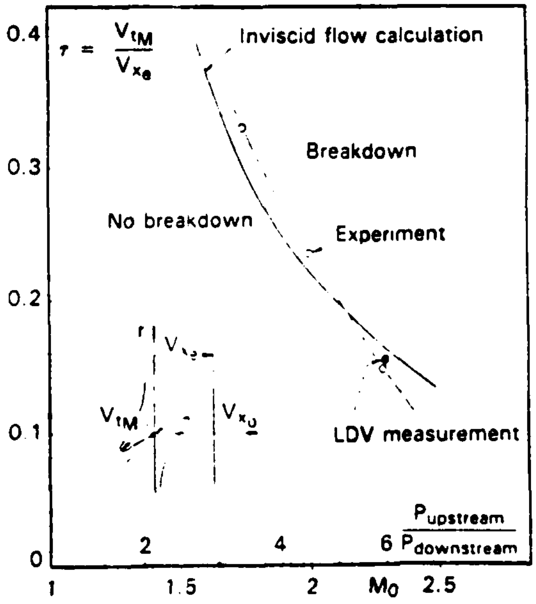

Fig. 2 Vortex breakdown curve. (From Ref. 2).

---

*Aerospace Engineer, Propulsion Group. Member AIAA.

**Professor, Aerospace Engineering Department. AIAA Fellow.

†There is one study in which the interaction between a vortex and a normal shock wave is examined (Ref. 2).

††Vortex breakdown is a phenomena wherein a vortex drastically changes its structure and takes on one of several new patterns. The restructuring is characterized by the information of a stagnation point on the vortex axis (Ref. 3).

The work contained in Reference 2 formed a basis for the input vortex used in our study. This will be discussed below. However, there is an obvious and fundamental difference between our work and Delery et al's investigations. In their studies the vortex encounters a subsonic flow after passing through the normal shock and while in our work the freestream flow is still supersonic after going through the oblique shock wave. This may be why no vortex breakdown was observed for the two SW/VI cases outlined below.

There are a variety of applications where shock wave/vortex interactions may take place. Figure 3 presents three examples. The first example, taken from Reference 2, shows a vortex/shock interaction on the leeward side of a delta wing. Modern supersonic aircraft and missiles require maximum maneuverability resulting in large angles of attack. This, in turn, results in strong vortices being shed from fins and wings. These vortices can have a significant impact on the vehicle performance and even safety (Ref. 4).

The second example shown in Figure 3, again from Reference 2, is that of a supersonic inlet ingesting a vortex. This is obviously an undesirable situation. A knowledge of the consequences of this interaction is necessary to judge the severity of the situation.

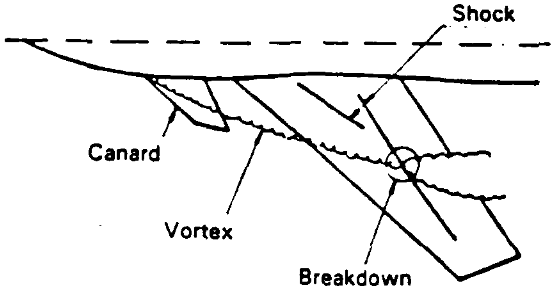

a) Transonic shock/vortex interaction (From Ref. 2).

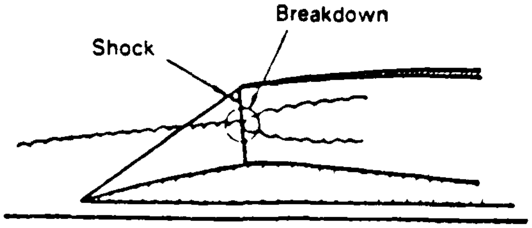

b) Supersonic Inlet (From Ref. 2).

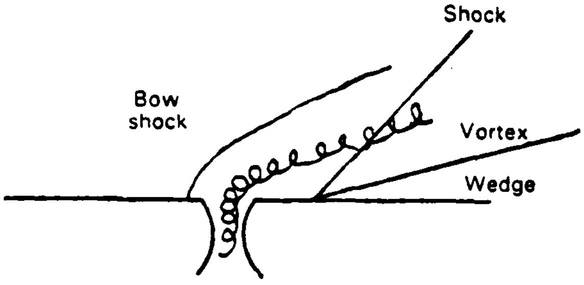

c) Injection into a supersonic flowfield.

**Fig. 3 Shock wave/vortex interaction applications.**

The third example presented in Figure 3 uses the interaction process to enhance mixing in a supersonic combustor. Whereas the first two examples are potentially undesirable situations, this illustrates a case where the interaction between a shock wave and a vortex may have a positive effect. The possibility of using SW/VI in this way was suggested to the first author by Dr. David Van Wie of the Johns Hopkins University Applied Physics Laboratory.

## Discussion

### The Numerical Model

The flowfield is approximated by numerically solving the Euler equations rather than the full Navier-Stokes equations. This was done for several reasons: 1) solving the Euler equations can be done at a fraction of the cost in code development and computer storage and run time over what is required to solve the full Navier-Stokes equations and 2) since very little research was found on the SW/VI process, a simple approach was desirable. A number of references were found in which the Euler equations were used successfully to model vortex dominated flowfields (see References 2, 5, 6). These references and our own experience justified the use of the inviscid equations for this problem.

After determining the class of equations to use it was necessary to choose a numerical model. The scheme chosen is based on the algorithm developed by Dr. Peter Gnoffo of the NASA Langley Research Center (Ref. 7). Gnoffo describes the model as:

> "... a robust, finite volume, single-level storage, implicit upwind differencing algorithm which has been documented and tested on several three-dimensional blunt body flows. The algorithm can run at unlimited Courant numbers but requires the inversion of only a 5 × 5 matrix per computational cell." (Ref. 7)

Our experience showed that the model was indeed robust, accurate, and capable of capturing shocks in a crisp manner.

The algorithm is briefly discussed below for completeness sake. A more detailed discription can be found in Reference 7. The model formulation begins with the integral form of the Euler or inviscid equations

$$\iiint_{\Omega_0} q_t \, d\Omega + \iint_{\sigma_0} \vec{f} \cdot \vec{n} \, d\sigma = 0 \tag{1}$$

$$\text{where } q_t = \frac{d}{dt}\begin{bmatrix}\rho \\ \rho u \\ \rho v \\ \rho w \\ \rho E\end{bmatrix}, \quad \vec{f} = \begin{bmatrix}\rho\vec{V} \\ \rho u\vec{V} + p\vec{i} \\ \rho v\vec{V} + p\vec{j} \\ \rho w\vec{V} + p\vec{k} \\ \rho E\vec{V} + p\vec{V}\end{bmatrix}, \quad \vec{n} = \begin{bmatrix}\vec{i} \\ \vec{j} \\ \vec{k}\end{bmatrix}$$

$\Omega$ = volume,
$\sigma$ = surface area,
$\rho$ = density,
$u, v, w$ = velocity components in the $\vec{i}, \vec{j}, \vec{k}$ directions,
$E$ = total energy per unit mass,
$\vec{V}$ = velocity vector,
$p$ = pressure,
$\vec{i}, \vec{j}, \vec{k}$ = the unit normal vectors.

Unlike finite difference methods which approximate the flowfield by a number a grid points, a finite volume method divides the flowfield up into cells. Equation (1) is then applied to a single cell within the flowfield resulting in the following approximate equation

$$\frac{\delta q_i \, \Omega_i}{\delta t} + \sum_{m=1}^{M_i} (g_{i+\frac{1}{2}} \cdot \sigma_{i+\frac{1}{2}})_m = 0 \tag{2}$$

where $\delta q_i = (q^{n+1} - q^{n})_i$,
$n + 1$,
$n$ = indicates the $n + 1$ and $n$ time step respectively
$i$ = indicates the ith cell,
$\Omega_i$ = the volume of cell $i$,
$\delta t$ = the time step,
$m$ = indicates the mth face of cell $i$,
$M_i$ = the number of faces surrounding cell $i$,
$g_{i+\frac{1}{2}}$ = $\bar{f}_{i+\frac{1}{2}} \cdot \hat{n}_{i+\frac{1}{2}}$,
$i + \frac{1}{2}$ = indicates the cell face between cells $i$ and $i + 1$,
$\sigma_{i+\frac{1}{2}}$ = the surface area between cells $i$ and $i + 1$.

The upwind differencing is introduced in the form of a second order dissipation term as follows:

$$g_{i+\frac{1}{2}} = .5\,[g_i + g_{i+1} - d_{i+\frac{1}{2}}(2)] \tag{3}$$

where $i$ = indicates the values at the cell center being evaluated,
$i + 1$ = indicates the values at the cell center of the neighboring cell which shares surface $i + \frac{1}{2}$,
$d_{i+\frac{1}{2}}(2)$ = the 2nd order dissipation term.

The second order dissipation term is taken from Helen Yee's paper, "Numerical Experiments with a Symmetric High-Resolution Shock-Capturing Scheme" (Ref. 8) and is defined as follows:

$$\begin{aligned} d_{i+\frac{1}{2}}(2) = {} & R_{i+\frac{1}{2}}^{-1}\, |L_{i+\frac{1}{2}}|\, \{R_{i+\frac{1}{2}}\, (q_{i+1}^{*} \\ & - q_i^{n}) - \text{minmod}[R_{i-\frac{1}{2}}\, (q_i^{n} - q_{i-1}^{*}),\ R_{i+\frac{1}{2}} \\ & (q_{i+1}^{*} - q_i^{n}),\ R_{i+3/2}\, (q_{i+2}^{*}) - q_{i+1}^{*})]\} \end{aligned} \tag{4}$$

The superscript $^*$ means to use the most recent values available. The diagonal matrix L is made up of the eigen values of matrix A (used to linearize dg with respect to dq), matrix R is made up of the right eigen vectors of matrix A, and matrix $R^{-1}$ is the inverse of R. The expressions for these matrices are developed using Roe's Property U (Ref. 9). A detailed evaluation of them can be found in Reference 7.

The model was validated by comparing its results to analytical solutions of 2-D flowfields such as a flowfield containing an oblique shock, a slip line intersecting an oblique shock, and two intersecting shock waves. These flowfields, although simple, provide a good test of the algorithm because the abrupt changes in the flow properties across the discontinuities typically cause shock smearing and down stream oscillations in flowfield properties.

Overall, the model results compared very well with analytical solutions. The numerical solution displayed crisp shocks with a minimal amount of smear and little downstream oscillation of the flow properties. The algorithm proved to be robust and converged quickly to a solution while doing a very good job of conserving mass, momentum, and energy. And as will be seen below, it also converges to a solution in very adverse flow situations, namely, the SW/VI flow.

It should be noted that for every case discussed below the solution demonstrated good global conservation of mass, momenutum, and energy. All cases where ran on the University of Maryland Univac 1190 computer using a flowfield containing 45360 cells (35 cells in the X-direction and 36 cells in the Y- and Z-directions).

## The Input Vortex

The nature of this study required that a vortex be provided as an upstream boundary to the flowfield. This input vortex would then sweep downstream as the solution was iterated in time. Therefore, it was necessary to find and/or develop a suitable input vortex.

As mentioned above, there has been surprisingly little work done detailing supersonic vortices. Only one reference was found which developed a useable input vortex, namely, Reference 2. The input vortex discussed in Reference 2 was derived by assuming uniform axial velocity, zero radial velocity, and constant total enthalpy. The tangential velocity, $V_t$, was described in terms of the classical Burgers' vortex:

$$\frac{V_t}{u_\infty} = \frac{K}{r}\left[1 - \exp\left(-\frac{r^2}{r_M^2}\right)\right] \tag{5}$$

where $u_\infty$ = the freestream velocity
$K$ = vortex strength parameter
$r$ = the radial direction
$r_M$ = vortex concentration

With the above assumptions and Equation 5, the radial momentum equation can be integrated for static pressure, thus, completely describing the vortex.

Two examples of the tangential velocity and pressure profiles resulting from the above development are illustrated in Figure 4 and compared with the experimental results of Delery et al. Notice that increasing $K$ increases the vortex strength, as expected.

To test this model, a vortex was input into a Mach 2.28 freestream and allowed to sweep downstream without the interference of a shock wave. The solution reached steady state in about 20 time steps. The pressure and density profiles from the steady state solution are illustrated in Figures 5 and 6. Other property profiles followed a similar trend. The solution shows the vortex changing with downstream distance indicating that the simple vortex model was not adequate. Curves A, B, C, and D represent profiles through the vortex at increasing distance downstream. This progressive weakening of the vortex was characteristic of all the vortices tested.

There appeared to be a slowing of the change in the vortex with downstream distance. Therefore, it was thought that inputting the final vortex profile from the outflow boundary as the upstream boundary in a new flowfield might lead to a converged vortex (one which did not change with downstream distance). As shown in Figures 7 and 8 this was indeed the case. The vortex clearly evolves to a converged solution. It was this final vortex that was then used as the upstream boundary for the Mach 2.28 SW/VI studies.

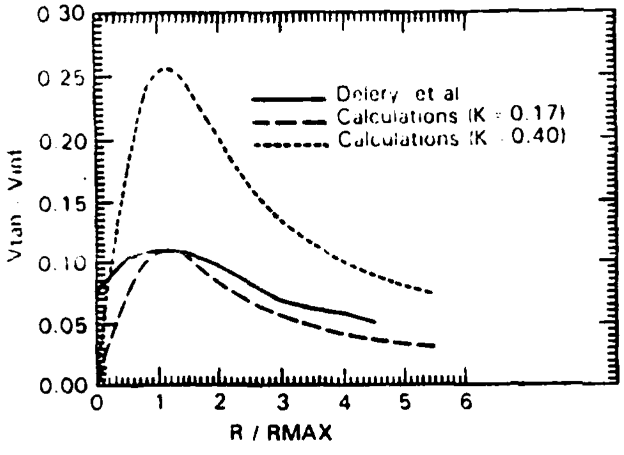

a) Tangential velocity profiles.

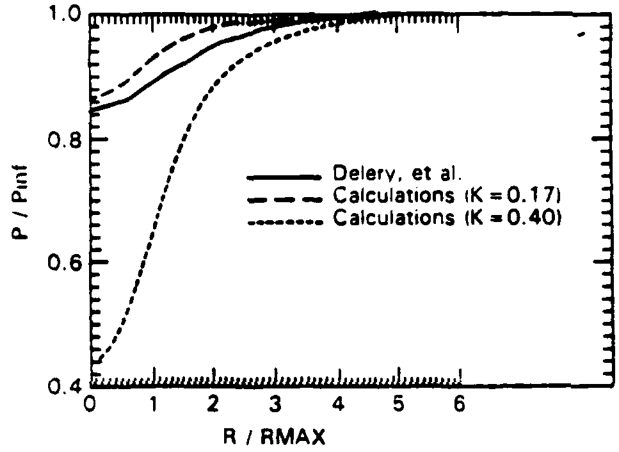

b) Pressure profiles.

**Fig. 4** Comparison between the experimental vortex profiles (Ref. 2) and the vortex model profiles for Mach = 2.28 and angle of attack = 10 degrees.

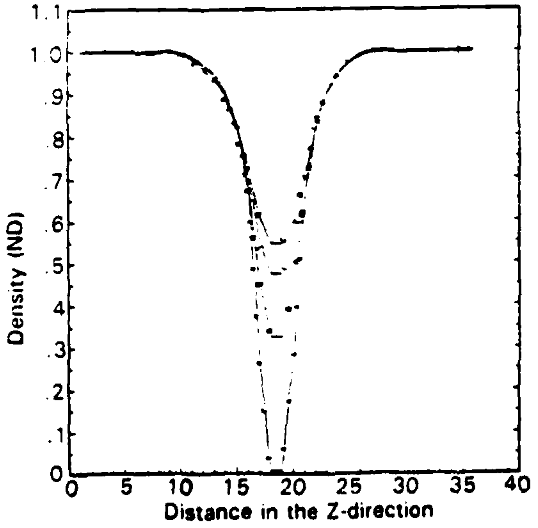

**Fig. 5** Vortex no. 2 density cross-section curves through the vortex center.

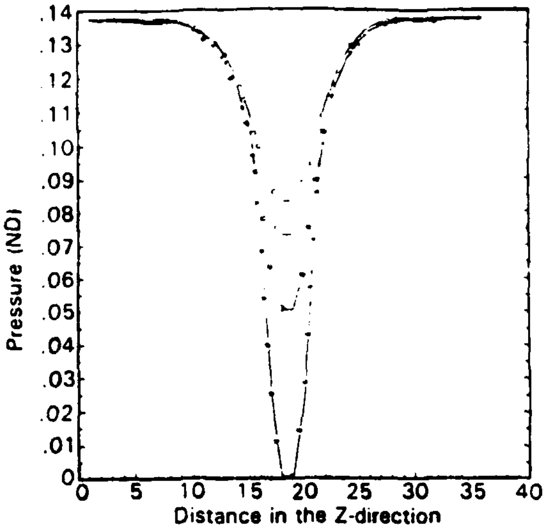

**Fig. 6** Vortex no. 2 pressure cross-section curves through the vortex center.

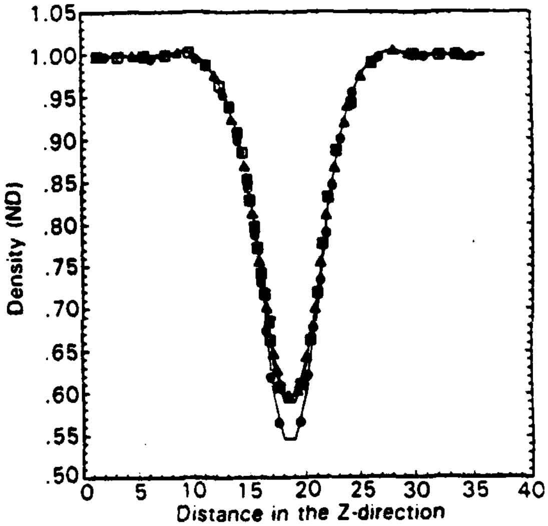

**Fig. 7** Vortex no. 2A density cross-section curves through the vortex center.

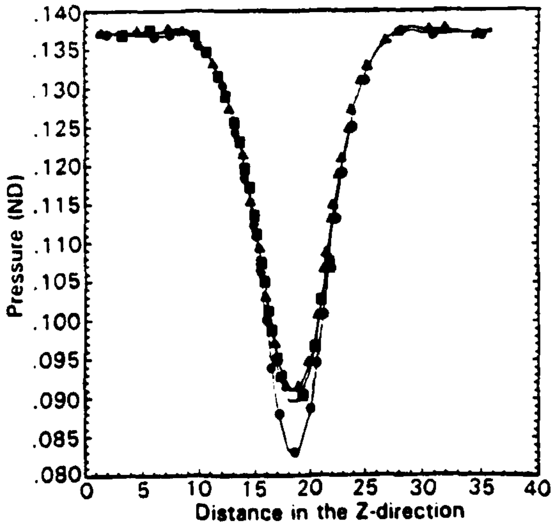

**Fig. 8** Vortex no. 2A pressure cross-section curves through the vortex center.

A similar approach was used in developing a vortex for the Mach 5.00 case. Unfortunately, unlike the Mach 2.28 case, the vortex never fully converged to a final profile. Figure 9 shows the density profiles through the vortex for 4 cycles. Each cycle takes the previous cycle's downstream vortex profile and uses it at an upstream profile. The vortex changes rapidly at first but then, rather than coverging, continues to change at a slow, steady rate. It was assumed that it would eventually dissipate totally. In spite of this anomaly, it was decided to use the vortex represented by curve D in Figure 9b for the Mach 5.00 SW/VI case.

The evolution of the simple vortices that were input to the final vortices that were output may be caused by a three-dimensional relieving effect. The input vortex model suggested by Delery et al (Ref. 2) is a simple 1-D solution to the Euler equations. It is likely that when the vortex is introduced into a three-dimensional field, it would weaken through the 3-D coupling of the governing equations. Since the vortices did eventually converge to a constant profile (or nearly constant profile), they were deemed adequate to use as input vortices for the SW/VI studies.

## The Shock Wave/Vortex Interaction Results

Understanding the results of the Mach 2.28 and 5.00 SW/VI flowfields is difficult because, through the interaction process, the flow becomes fully three-dimensional. Inherent in this difficulty is trying to visualize the 3-D results on a 2-D medium.

To aid in the process, streamline and contour plots will be used along with cross-sections curves of parameters cut through the contour plots. Each contour plot can be taken perpendicular to all three axes and perpendicular to the freestream flow behind the oblique shock wave. The cross-section curves can be cut across the contour plot perpendicular to each of the two axes. It quickly becomes apparent that the examination of a three dimensional flowfield is a complex and laborious process.

Keep the following in mind when viewing the plots: Each contour plot will usually have two inserts which will schematically show the location and orientation of the figure with regards to the rest of the flowfield. Figure 1 shows the orientation of the axes. The contour and streamline plots will be shown in the Y-Z plane only and are viewed as if the observer were standing along the negative X-axis looking in the positive X direction.

In discussing the flowfield solution it is necessary to understand the swirl direction of the vortices. The vortices in this study swirl in a counter-clockwise direction when viewed as if one were standing on the negative X-axis looking in the positive X direction. The left and right side of the vortex refer to the vortex when viewed from the negative X-axis looking in the positive X direction.

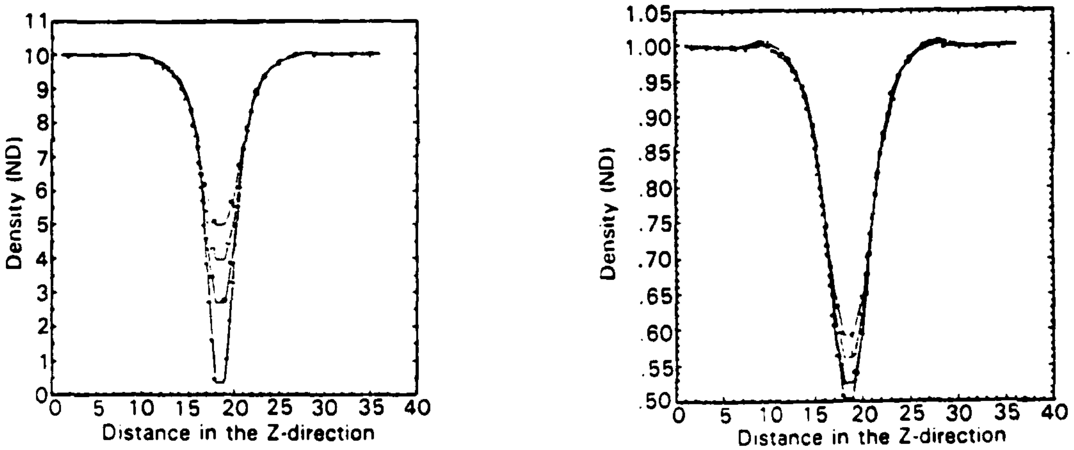

a) Cycle 1 — vortex 3 to 3A

b) Cycle 2 — vortex 3A to 3B

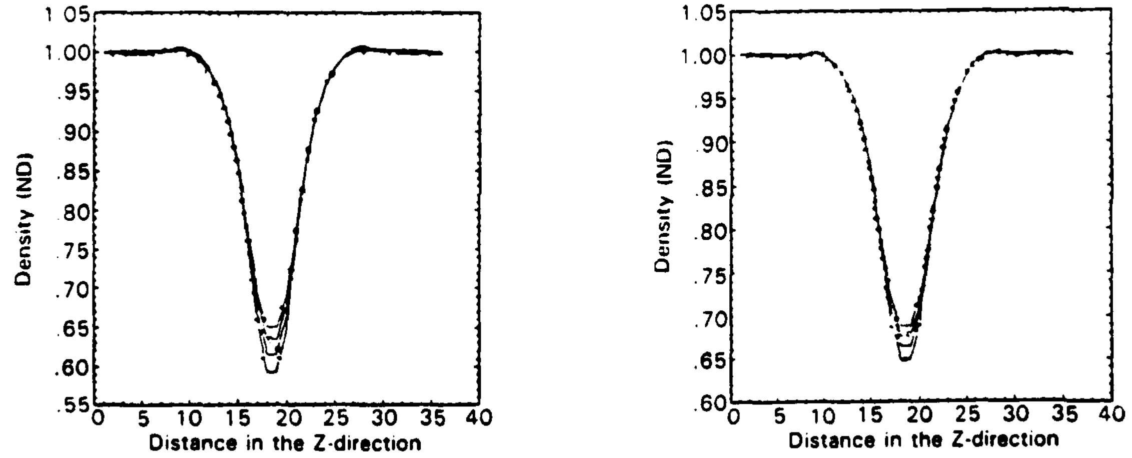

c) Cycle 3 — vortex 3B to 3C

d) Cycle 4 — vortex 3C to 3D

**Fig. 9 Density cross-section curves through the vortex center for 4 different cycles.**

### Shock Wave/Vortex Interaction Case No. 1

The first case, designated SW/VI Case No. 1, introduces the vortex discussed above into a Mach 2.28 flowfield containing an oblique shock wave resulting from a wedge angle of 20 degrees. Figures 10 and 11 show the density contour plots at various locations along the X-axis. Figures 12 and 13 show density cross-section curves through the post-shock vortex.

Four observations can be made based on the density plots:

1) The vortex did not break down after passing through the shock wave.

2) The shock surface develops a convex-concave shape.

3) A fairly coherent area of high density has developed to the left of the vortex at the point where the vortex passes through the shock wave. This area continues downstream along with the vortex.

4) A large area of low density developed on the right side of the vortex after it passed through the shock wave. This area almost encompasses the vortex in the last plane.

5) The vortex is deflected to the left after passing through the shock.

The pressure and Mach number plots are presented in Reference 1 and echo these observations. The cause of these effects is due to the fact that the velocity component on each side of the vortex intersects the shock wave at different angles. This results in a shock curvature across the vortex and the corresponding difference in the properties across the shock on the two sides of the vortex.

Figures 14 and 15 show the post-shock axial contour plot and the tangential velocity streamline plot, respectively. Finally, Figures 16 and 17 are cross-section curves corresponding to Figures 14 and 15. Notice the asymmetrical shape of the axial and tangential profiles. This is to be expected, again, because the velocity vector intersects the oblique shock wave at different angles on the right and left sides of the vortex.

Although, the asymmetry was expected, the appearance of several streamlines running opposite the main vortex streamlines was not expected. These streamlines suggest the formation of regions of reversed flow and can be seen along the outside of the vortex shown in Figure 15. The reversed flow to the right of the main vortex can also be seen in the tangential velocity profiles as a dip in the profile.

The cause of this reversed flow is unknown, however, it may be due to vorticity generation due to the nonuniform pre-shock flowfield and the shock curvature. More study is needed to confirm this.

### Shock Wave/Vortex Interaction Case No. 2

The second case, designated SW/VI Case No. 2, introduces the above discussed Mach 5.00 vortex into a a flowfield containing an oblique shock wave resulting from a wedge angle of 32.8 degrees.

This flowfield will be harder to analyze than the previous case for two reasons. The first reason is because of the smaller distance between the shock and the vortex at the outflow plane due to the decreased angle between the shock and the post-shock freestream flow. Thus, the part of the flowfield of interest is contained in a smaller area. Additionally, the changes in the properties across the shock are greater than for Case No. 1 which tends to wash out the more subtle changes.

Paralleling the plots shown for the case above, Figures 18 and 19 show the density contour plots at various locations along the X-axis. Figures 20 and 21 show density cross-section curves through the post-shock vortex. Figures 22 and 23 show the post-shock axial contour plot and the tangential velocity streamline plot, respectively. Figures 24 and 25 are cross-section curves corresponding to Figures 22 and 23.

It is obvious after looking at the density plots that there will be a lack of detail in the graphics. Case No. 1, however, provides some clues as to what to look for. There were some similarities and one unusual difference between the two solutions. The difference is a trough encompassing the main vortex after it passes through the shock which is in addition to the high and low areas seen in Case No. 1. The following summarizes the observations:

1) There is a trough that appears to encompass the main vortex after the vortex passes through the shock.

2) Regions of reversed flow appear outside of the main vortex.

3) The vortex has not broken down.

4) The shock curvature, the areas of high and low properties, and the vortex deflection noted in Case No. 1 are again present.

The presence of the trough in this case and not in Case No. 1 is most peculiar. It may be due to the formation of a slip surface developed while the vortex is passing through the shock wave or it may be a Mach number phenomena caused by the increased shock strength in this case. It may also be related to the regions of reversed flow. Again, more study is needed to fully understand this phenomena.

### Conclusion

This concludes the discussion of the shock wave/vortex interaction studies. The two cases have shown a variety of interesting results. A most important conclusion of this study is that the vortex did not breakdown in either case. Although it was not noted above, the vortex strength did not change appreciably in either case after passing through the shock wave. This may be why neither vortex broke down. Related to this may be the fact that the post-shock freestream flow is supersonic.

Both solutions showed the expected shock curvature and areas of high and low properties on the outside of the main vortex. In addition to these effects, in each case, the vortex was deflected to the left as it passed through the shock wave.

There were two unexpected and fascinating results of the study. The first one, common to both solutions, was the formation of regions of reversed flow after the main vortex passed through the shock wave. These structures seen in the respective streamline plots and the tangential velocity profiles across the post-shock vortex are a puzzle. The cause of the structures is unknown. It is hypothesised that they may be the result of vorticity generation due to the nonuniform pre-shock flowfield and the shock curvature.

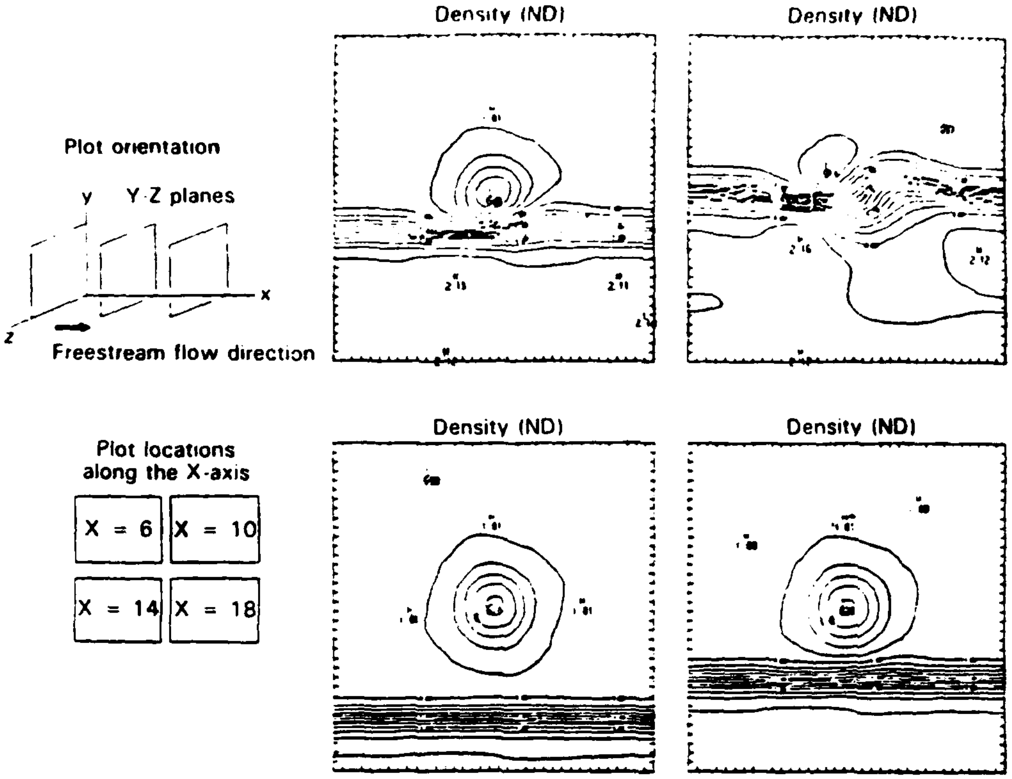

**Fig. 10** SW/VI case no. 1 density contour plots in the Y-Z plane and at X-locations 6 to 18.

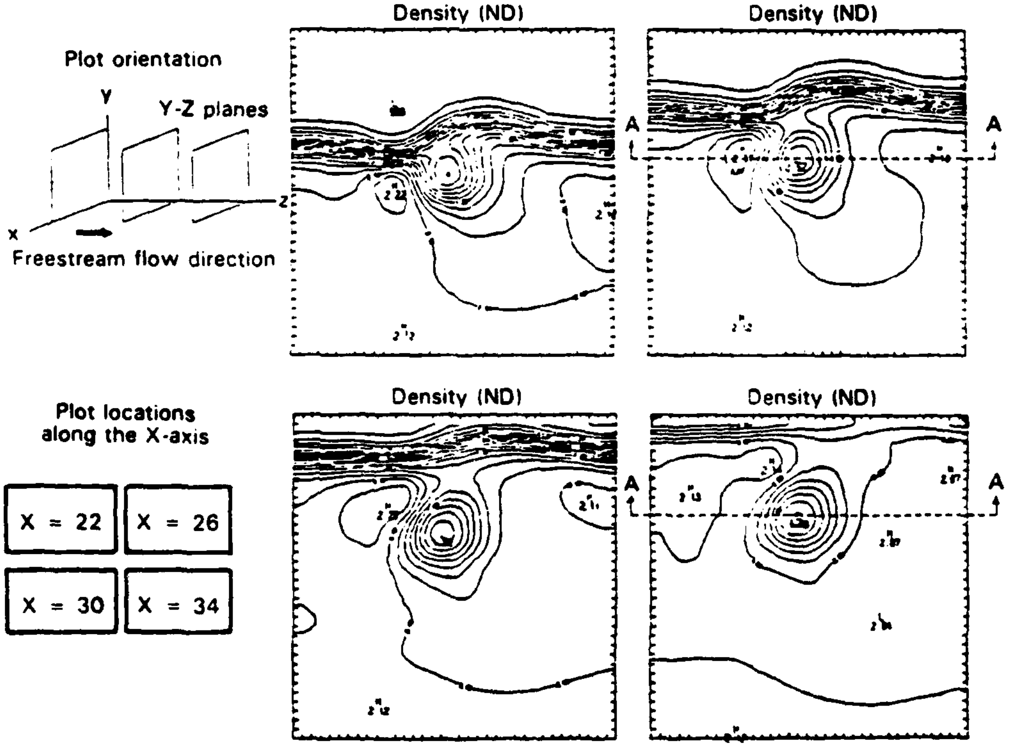

**Fig. 11** SW/VI case no. 1 density contour plots in the Y-Z plane and at X-locations 22 to 34.

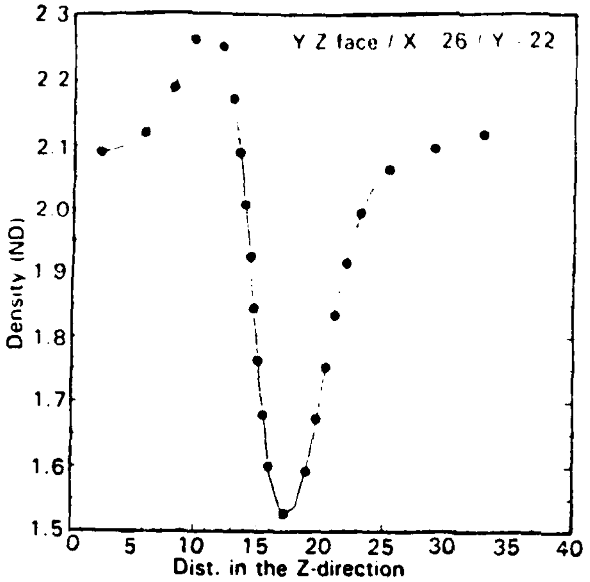

Fig. 12 SW/VI case no. 1 density cross-section curve in the Y-Z plane, in the Z-direction, through the vortex center, and at X-location = 26.

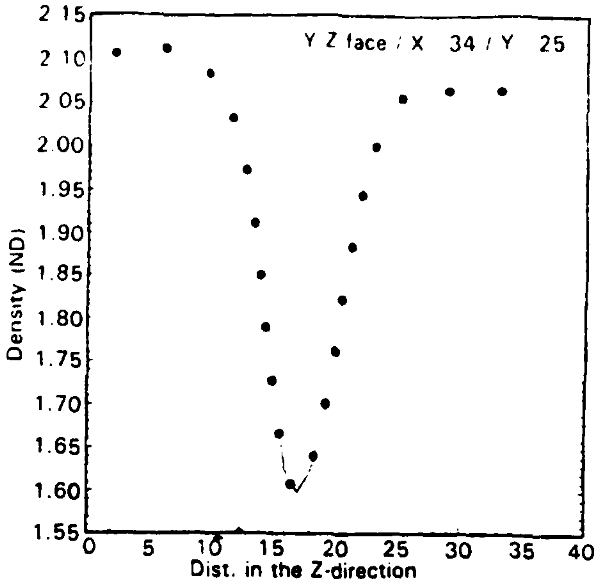

Fig. 13 SW/VI case no. 1 density cross-section curve in the Y-Z plane, in the Z-direction, through the vortex center, and at X-location = 34.

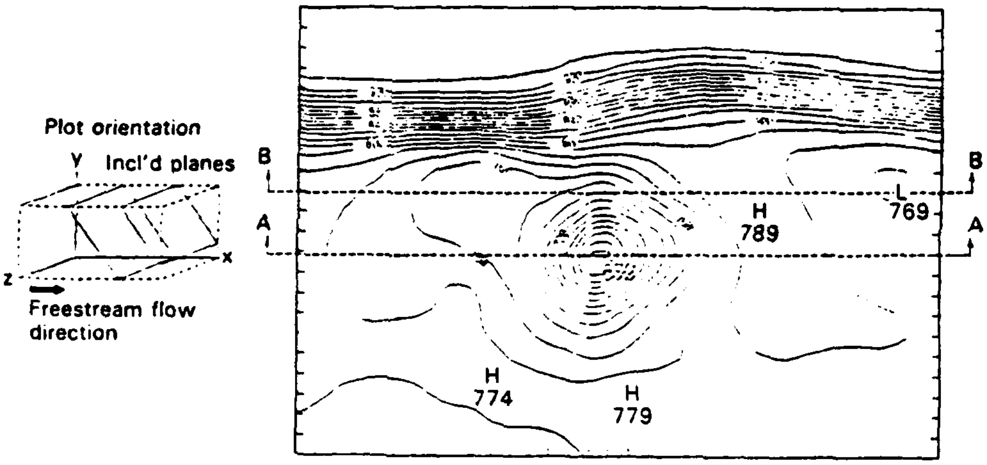

Contour from .55088 to .930100 contour interval of 10000-001 pt(3,3) = .76821

Fig. 14 SW/VI case no. 1 post-shock axial velocity contour plot in the 110 deg. plane and beginning at Y-location = 15.

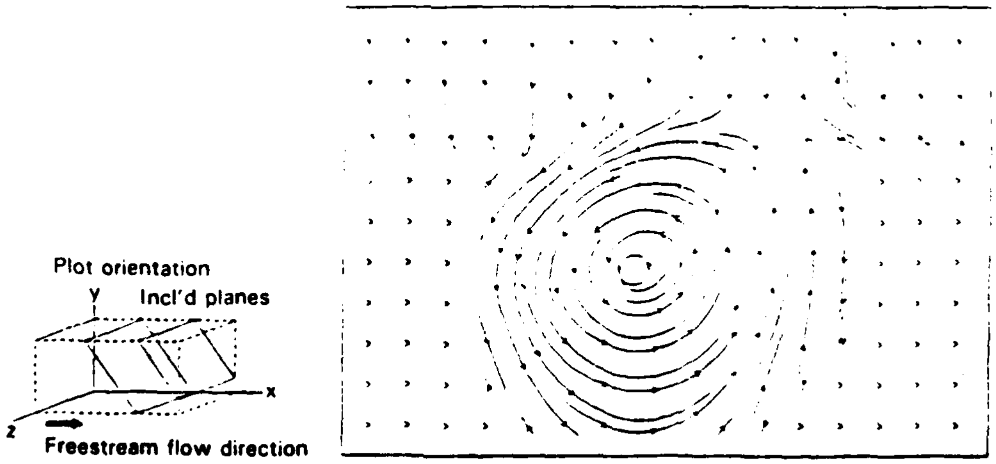

Fig. 15 SW/VI case no. 1 post-shock tangential velocity streamline plot in the 110 deg. plane and beginning at Y-location = 15.

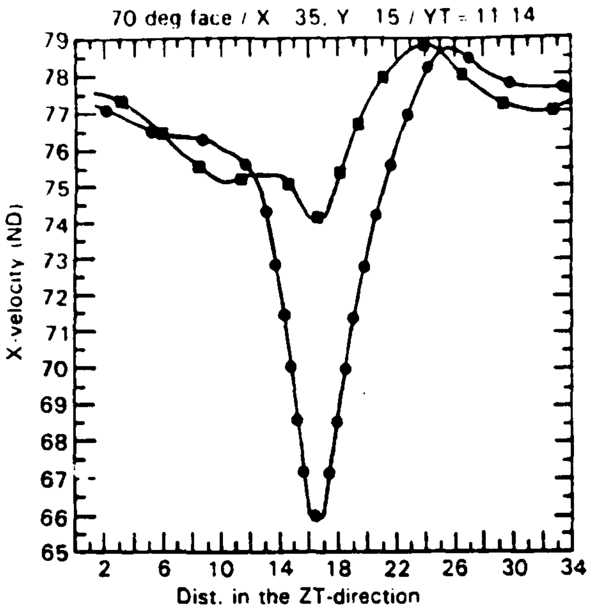

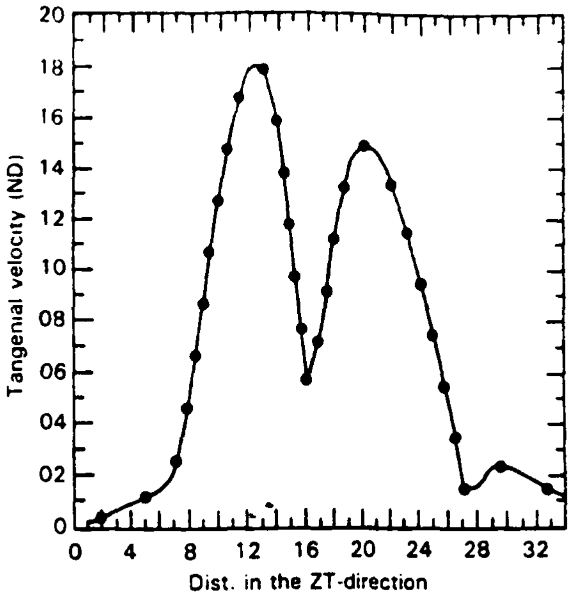

**Fig. 16** SW/VI case no. 1 post-shock axial velocity cross-section curve in the 110 deg. plane and beginning at Y-location = 15.

**Fig. 17** SW/VI case no. 1 post-shock tangential velocity cross-section curves in the 110 deg. plane, through the vortex center, and beginning at Y-location = 15.

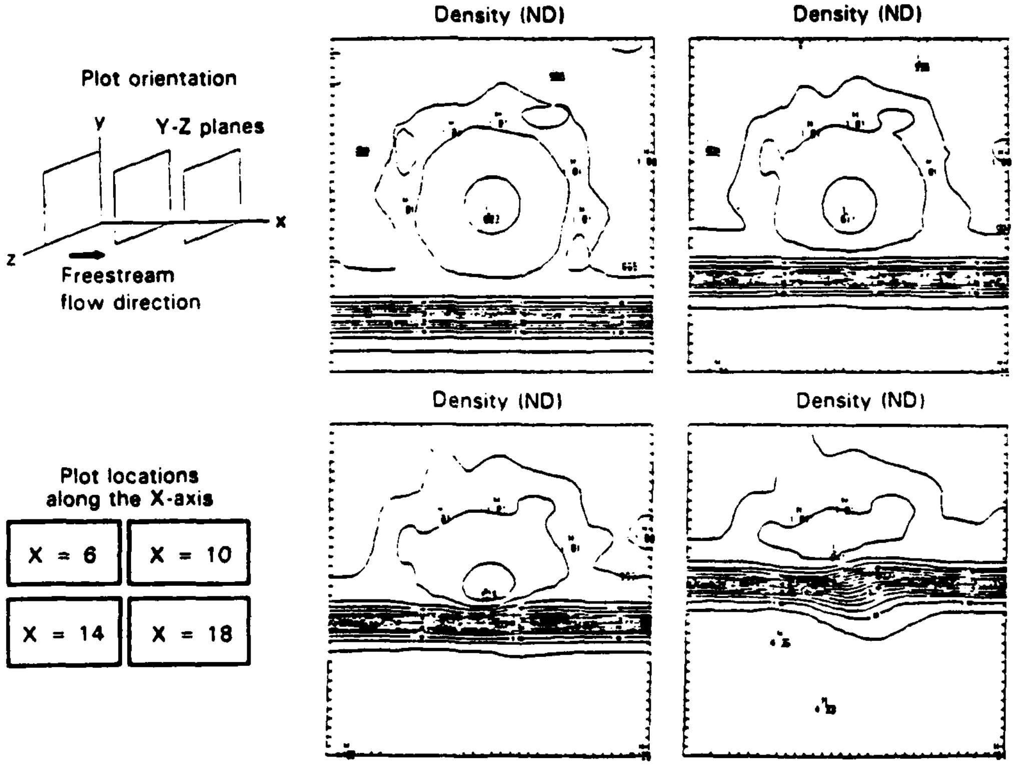

**Fig. 18** SW/VI case no. 2 density contour plots in the Y-Z plane and at X-locations = 6 to 18.

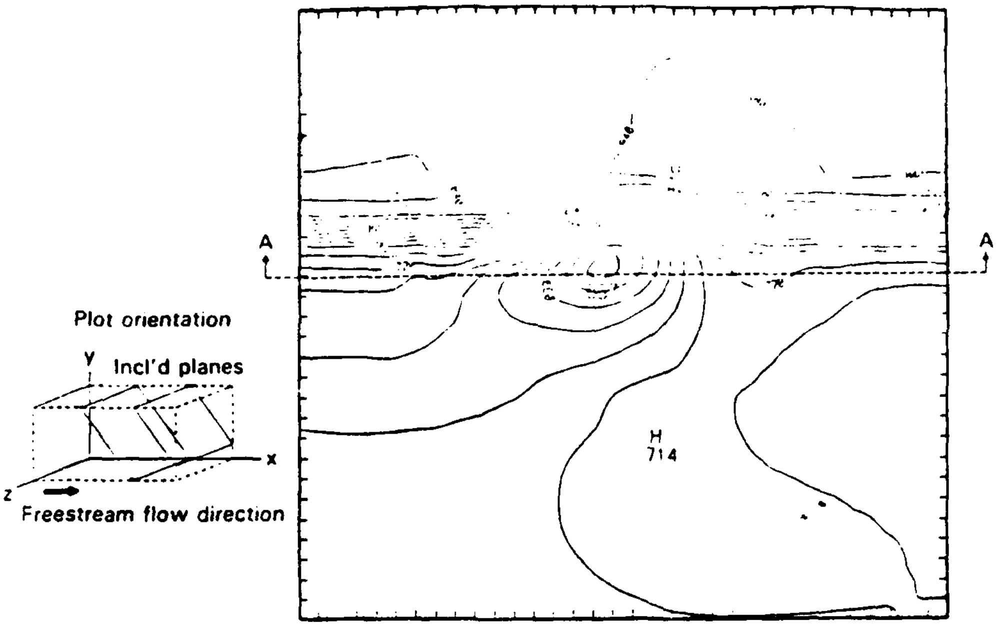

Contour from 66000 to 84000 contour interval of
10000-001 PT(3,3) = .70941

**Fig. 22** **SW/VI case no. 2 post-shock axial velocity contour plot in the 123 deg. plane and beginning at Y-location = 10.**

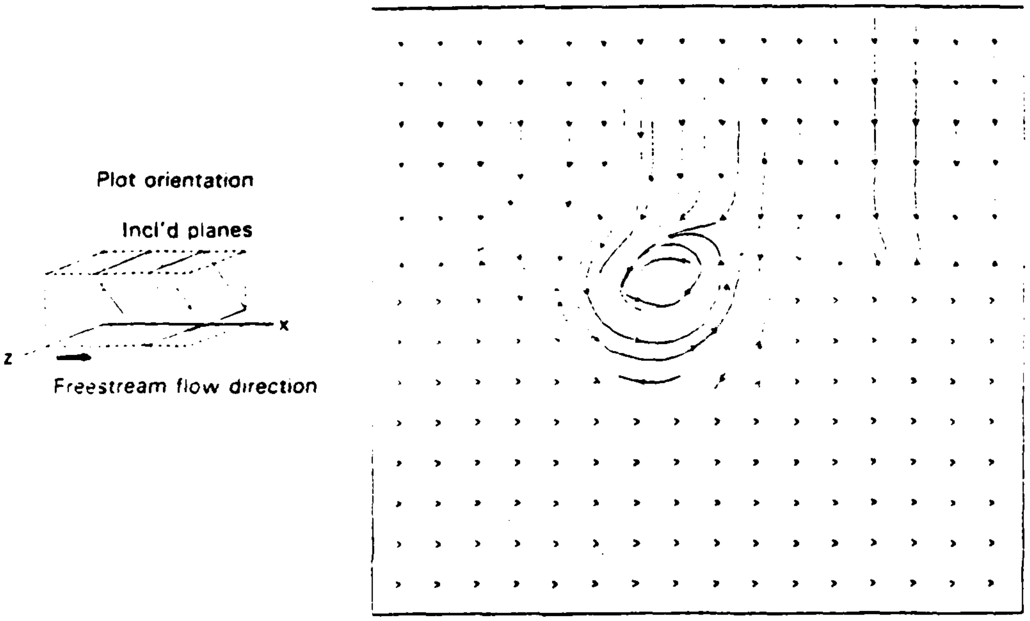

**Fig. 23** **SW/VI case no. 2 post-shock tangential velocity streamline plot in the 123 deg. plane and beginning at Y-location = 10.**

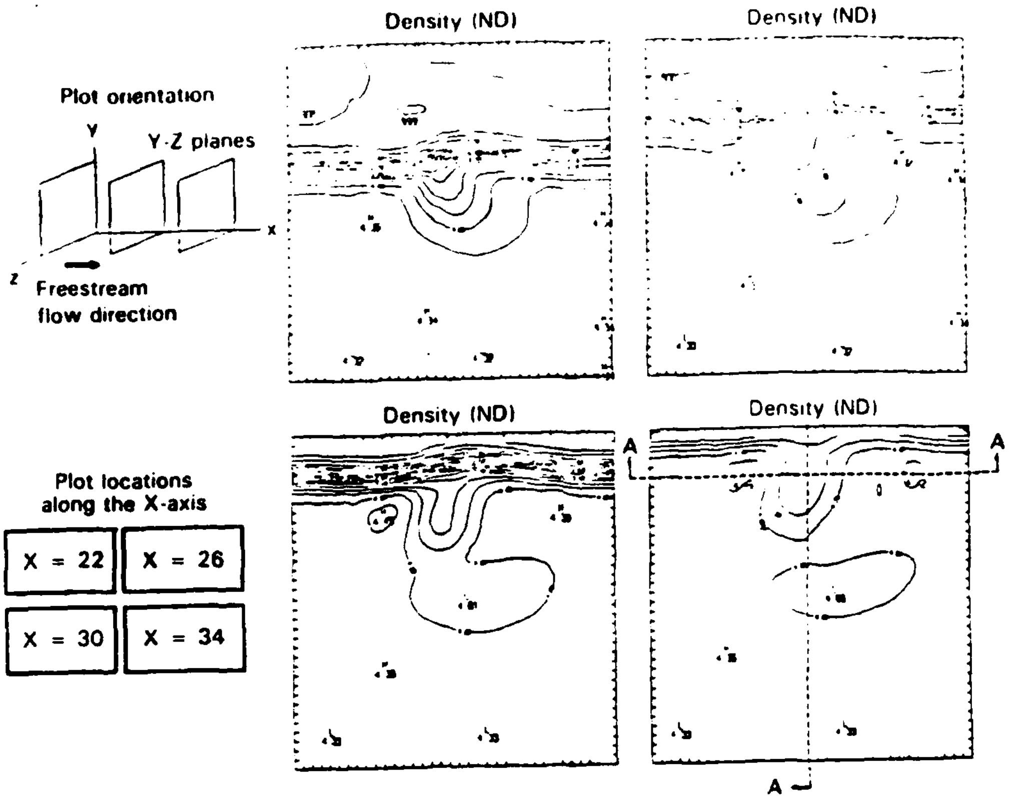

Fig. 19 SW/VI case no. 2 density contour plots in the Y-Z plane and at X-locations = 22 to 34.

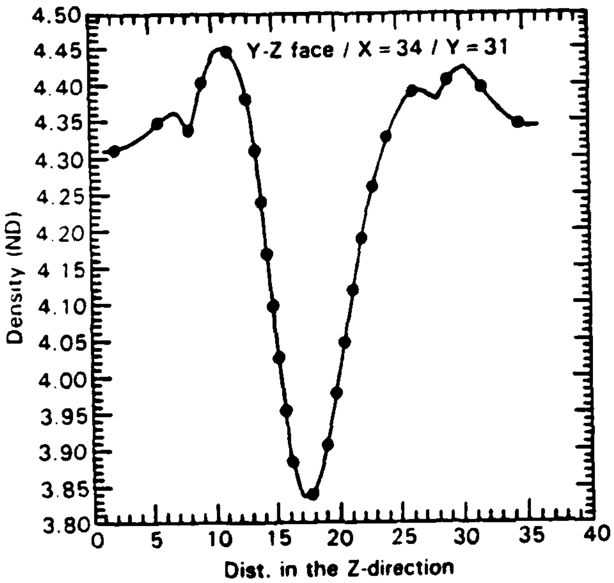

Fig. 20 SW/VI case no. 2 density cross-section curve in the Y-Z plane, in the Z-direction, through the vortex center, and at X-location = 34.

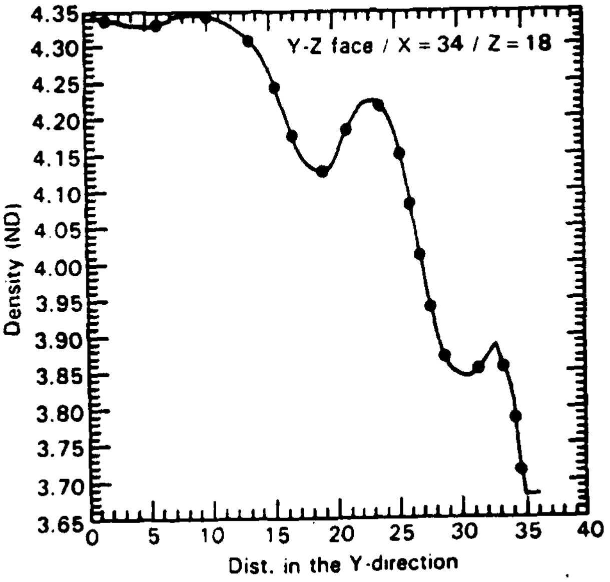

Fig. 21 SW/VI case no. 2 density cross-section curve in the X-Y plane, in the Y-direction, through the vortex center, and at X-location = 34.

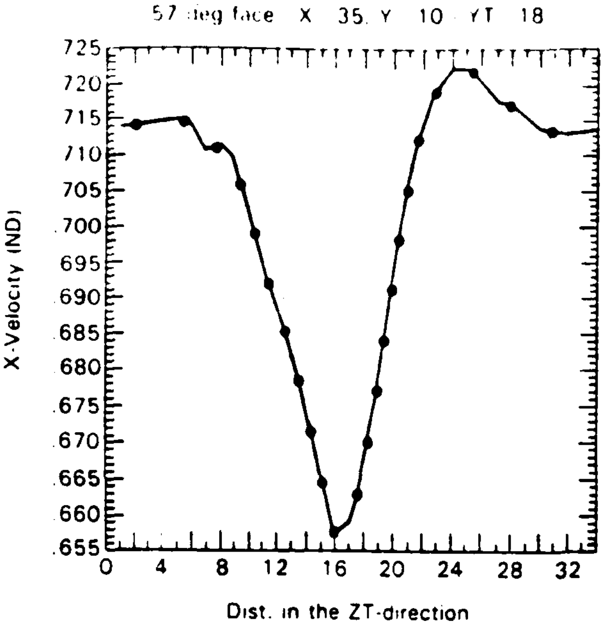

**Fig. 24 SW/VI case no. 2 post-shock axial velocity cross-section curve in the 123 deg. plane, through the vortex center, and beginning at Y-location = 10.**

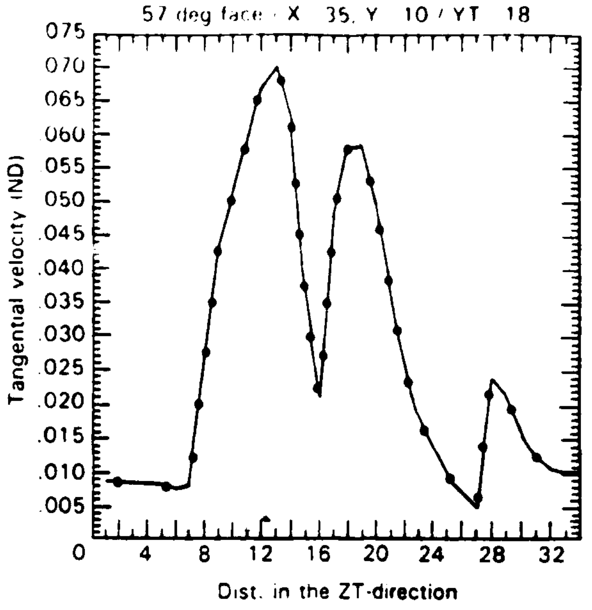

**Fig. 25 SW/VI case no. 2 post-shock tangential velocity cross-section curves in the 123 deg. plane, through the vortex center, and beginning at Y-location = 10.**

The other unexpected result was observed in the second case, but not in the first. It was the formation of a trough surrounding the main vortex after it passed through the shock. This phenomena could be related to the above mentioned reversed flow regions or it may be caused by the formation of a slip-line like surface.

In any event, the surprising phenomena observed as a result of the numerical solution to these flowfields, namely the areas of reversed flow and the trough structure, have not been documented before to the best of the authors' knowledge. However, caution must be used in drawing conclusions. This has been a preliminary study of a very complex interaction flowfield using, by necessity, a fairly simple approach. The results must be weighed against this approach. It is hoped that these initial findings will generate further interest and study which will, in turn, either support or challenge the results. Only through more analytical, experimental, and computational study will this flowfield be fully understood.

## References

1. Corpening, G. P., Numerical Solutions to Three-Dimensional Shock Wave/Vortex Interaction at Hypersonic Speeds, Ph.D. Disseration, University of Maryland, College Park, Maryland, 1988.

2. Delery, J., Horowitz, E., Leuchter, O., and Solignac, J.-L., "Fundamental Studies on Vortex Flows," La Recherche Aerospatiale (English Edition) (ISSN 0379-380X), No. 2, 1984.

3. Leibovich, S., "The Structure of Vortex Breakdown," Annual Review of Fluid Mechanics, Vol. 10, 1978, pp. 221-246.

4. Newsome, R. W. and Kandil, O. A., "Vortical Flow Aerodynamics - Physical Aspects and Numerical Simulation," AIAA Paper No. 87-0205, Jan. 1987.

5. Rizzetta, D. P. and Shang J. S., "Numerical Simulation of Leading-Edge Vortex Flows," AIAA Journal, Vol. 24, No. 2, Aug. 1986, pp. 237-245.

6. Weiland, C., "Vortex Flow Simulations Past Wings Using the Euler-Equations," Aerodynamics of Vortical Type Flows in Three Dimensions, AGARD-CP-342, Apr. 1983, pp. 19-1 – 19-12.

7. Gnoffo, P. A., "Application of Program LAURA to Three-Dimensional AOTV Flowfields," AIAA Paper No. 86-0565, Jan. 1986.

8. Yee, H. C., "Numerical Experiments with a Symmetric High-Resolution Shock-Capturing Scheme," NASA TM-88325, Jun. 1986.

9. Roe, P. L., "Approximate Reimann Solvers, Parameter Vector, and Difference Schemes," Journal of Computational Physics, Vol 43, 1981, pp. 357-372.

# DISCLAIMER NOTICE

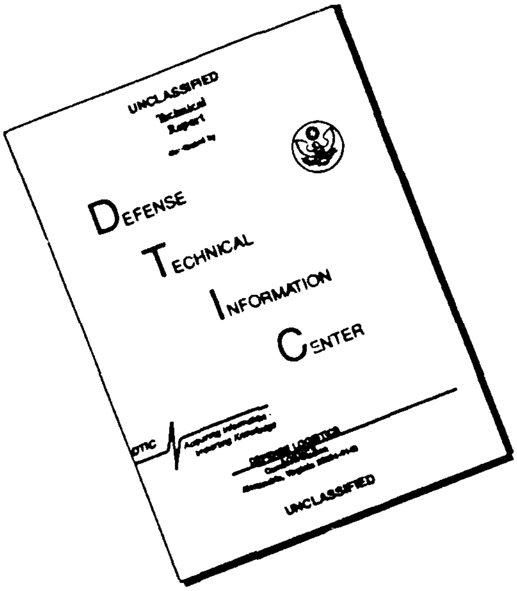

UNCLASSIFIED

DEFENSE

TECHNICAL

INFORMATION

CENTER

DTIC

UNCLASSIFIED